HETEROCYCLES, Vol. 100, No. 8, 2020, pp. 1123-1162. © 2020 The Japan Institute of Heterocyclic Chemistry
Received, 2nd March, 2020, Accepted, 25th March, 2020, Published online, 9th April, 2020
DOI: 10.3987/REV-20-927

5,15-DIHETEROPORPHYRINS SYNTHESIZED FROM α,α'-DIHALODIPYRRIN AS A KEY BUILDING BLOCK

Soji Shimizu[a,b]*

[a]Department of Chemistry and Biochemistry, Graduate School of Engineering, Kyushu University, Fukuoka 819-0395, Japan, ssoji@cstf.kyushu-u.ac.jp
[b]Center for Molecular Systems (CMS), Kyushu University, Fukuoka 819-0395, Japan

Abstract – A facile synthesis of *meso*-aryl-substituted α,α'-dihalodipyrrins and their use as starting materials in the porphyrin synthesis have enabled creation of various porphyrin analogues containing heteroatoms at two opposite *meso*-positions, namely 5,15-positions. Incorporation of lone pair electrons into the 18π-electron aromatic conjugated system of porphyrin allows the system to attain antiaromaticity with unique optical and electrochemical properties. This review summarizes the recent development in the chemistry of 5,15-diheteroporphyrins synthesized from *meso*-aryl-substituted α,α'-dihalodipyrrins.

CONTENTS

1. INTRODUCTION

Porphyrin is a naturally occurring functional molecule, the structure of which can be seen as heme in mammalian blood and chlorophyll in plants.[1–3] It consists of four pyrrole rings connected to each other by a methine carbon at the *meso*-position to form an 18π-aromatic conjugated system (Figure 1).

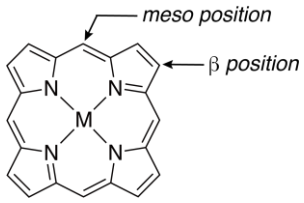

Figure 1. Structure of porphyrin

In the early stage of porphyrin chemistry, it was found that a 5-oxaporphyrin derivative called verdoheme, in which one of the methine carbon atoms is replaced with an oxygen atom, is metabolized during the heme catabolism (Scheme 1).[4–8] The initial study of this kind of heteroatom-containing porphyrin analogues (heteroporphyrins) focused on elucidation of the reaction mechanism and chemical modification of this metabolite via an open-chain derivative called biliverdin to replace the central metal ions[9–11] and the *meso*-oxygen atom with other heteroatoms, such as nitrogen and sulfur (Scheme 2).[12,13]

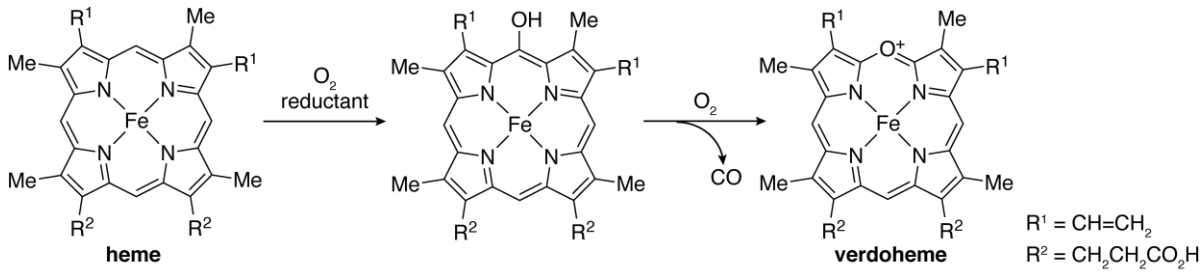

Scheme 1. Verdoheme metabolism from heme

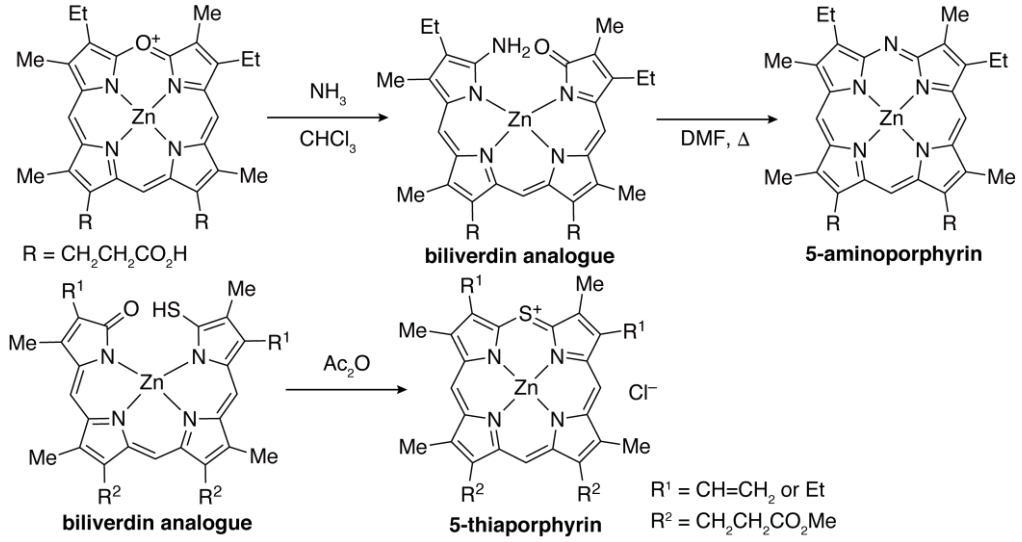

Scheme 2. 5-Heteroporphyrins synthesized from biliverdin analogues

Balch and co-workers, then, developed the bioinspired synthesis of iron and cobalt complexes of 5-oxaporphyrin by oxidation of an iron(II) complex of octaethylporphyrin (Scheme 3).[14–18] Later on, Mizutani and co-workers reported that *meso*-aryl-substituted 5-oxaporphyrin can be derived from *meso*-tetraaryl-substituted iron(II) porphyrin via an oxidized open-chain 5,10,15-triarylbilindione intermediate (Scheme 4).[19–21] In addition to heteroporphyrins, the contracted corrole analogues called heterocorroles were also investigated by Johnson and co-workers (Scheme 5).[22]

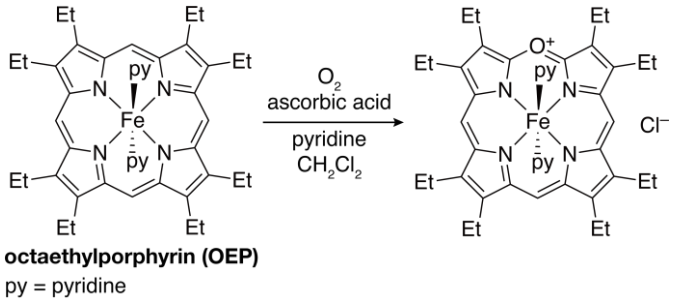

Scheme 3. Bioinspired synthesis of 5-oxaporphyrin from octaethylporphyrin

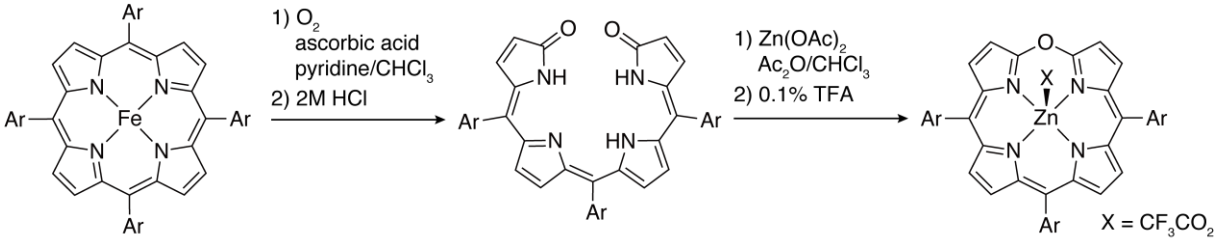

Scheme 4. Synthesis of *meso*-aryl-substituted 5-oxaporphyrin from *meso*-tetraaryl-substituted porphyrin

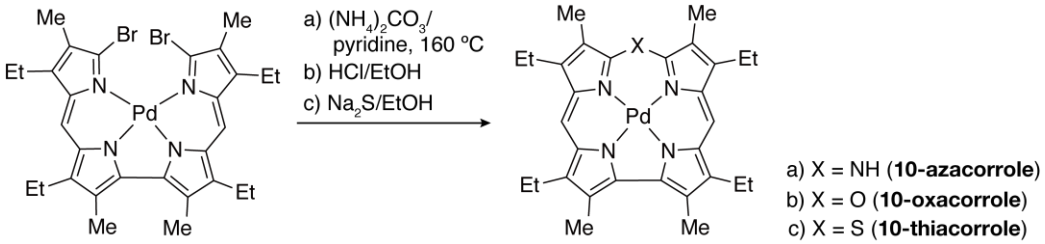

Scheme 5. Synthesis of heterocorroles

Despite these pioneering investigations, there has been a rather sparse number of reports on heteroporphyrins until recently. In 2012, the breakthrough in the synthesis of heteroporphyrins was independently made by Matano and Shinokubo, who used a bis(*meso*-aryl-substituted α,α'-dihalodipyrrin) nickel complex in the synthesis of 10,20-diaryl-5,15-diazaporphyrin (Schemes 6 and 7).[23,24] In addition to 5,15-diazaporphyrin, Shinokubo and co-workers found that 10-azacorrole was also formed under the Buchwald-Hartwig amination reaction conditions.[24]

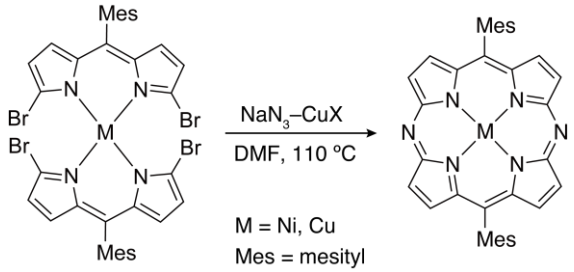

Scheme 6. Synthesis of 10,20-diaryl-5,15-diazaporphyrin using sodium azide

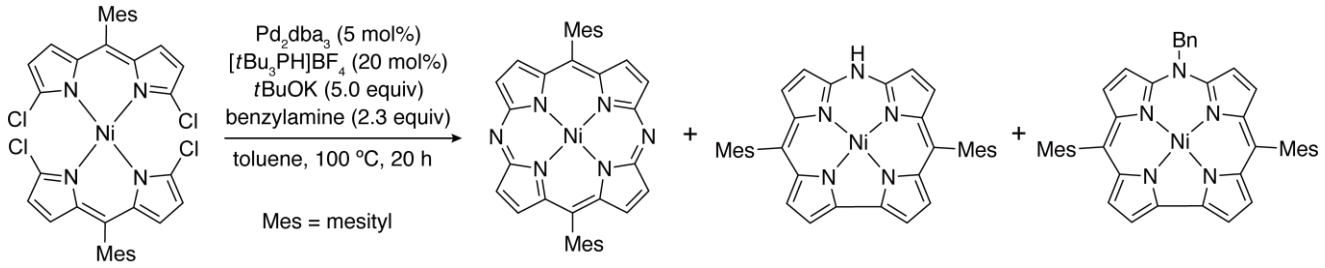

Scheme 7. Synthesis of 10,20-diaryl-5,15-diazaporphyrin and 5,15-diaryl-10-azacorroles under the Buchwald-Hartwig amination reaction conditions

Owing to the recent development of the facile synthesis of *meso*-aryl-substituted α,α'-dihalodipyrrin compared with that of β-alkyl-substituted one, a series of 5,15-diheteroporphyrins containing nitrogen, oxygen, and sulfur atoms has been synthesized in recent years (Figure 2).[25] Among them, nitrogen- and oxygen-containing analogues exhibit antiaromatic characters due to incorporation of lone pair electrons of heteroatoms into the main conjugation pathways. Because such antiaromatic 5,15-diheteroporphyrins are stable under ambient conditions, unlike other antiaromatic porphyrin analogues such as isophlorin (Figure 2),[26] *meso*-heteroatom-substitution using *meso*-aryl-substituted α,α'-dihalodipyrrin can be regarded as a rational synthetic strategy to create stable antiaromatic porphyrin analogues.

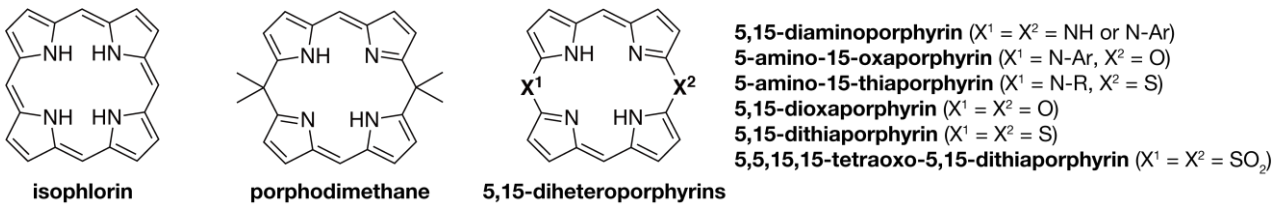

Figure 2. Structures of isoporphyrin, porphodimethane, and 5,15-diheteroporphyrins

In this review, the recent progress in the chemistry of 5,15-diheteroporphyrins synthesized from *meso*-aryl-substituted α,α'-dihalodipyrrin is summarized. In terms of molecular structures, 5,15-diheteroporphyrin can be regarded as heteroatom analogues of porphodimethane,[27] which is conventionally called calixphyrin (Figure 2). Although partially *meso*-nitrogen-substituted azaporphyrin analogues[28–34] such as 5,15-diazaporphyrin (Schemes 6 and 7)[23,24,35–37] and 5,10,15-triazaporphyrin[38] can

also be synthesized from *meso*-aryl-substituted α,α'-dihalodipyrrin, such kind of azaporphyrin analogues are excluded in this review because they are more suitably categorized as heteroatom-containing porphyrin analogues. Comprehensive review by Matano in 2017 covers all kinds of azaporphyrin analogues.[25] Instead, the latest examples until the early 2020 are included in this review. For compound names of azaporphyrins bearing amino nitrogen atoms, instead of using "aza", "amino" is used to distinguish, for example, between 5,15-diaminoporphyrin with amino nitrogen atoms and 5,15-diazaporphyrin with imino nitrogen atoms.

Aromaticity/antiaromaticity is a key property of 5,15-diheteroporphyrins. In addition to chemical shifts of NMR spectra and theoretical calculations, such as nucleus-independent chemical shift (NICS),[39] anisotropy of the induced current density (ACID),[40] and gauge-including magnetically induced current (GIMIC),[41,42] UV/vis absorption and magnetic circular dichroism (MCD) spectral profiles are diagnostic of aromatic and antiaromatic porphyrin analogues. Therefore, the theoretical description of absorption properties of porphyrin and related analogues is briefly introduced in the next chapter.

2. THEORETICAL ABSORPTION DESCRIPTION OF AROMATIC AND ANTIAROMATIC PORPHYRIN ANALOGUES

2-1. Gouterman's four orbital theory and absorption properties of porphyrin and related analogues

UV/vis absorption spectra of porphyrins exhibit diagnostic bands called Soret and Q bands. As shown in Figure 3, the Q band is observed around 500–650 nm as a weak, forbidden band, whereas the intense, allowed Soret band appears in the higher energy region around 400 nm. In his seminal work known as Gouterman's four orbital theory, Gouterman successfully described the difference in energy and intensity between the Soret and Q bands using four frontier orbitals, HOMO, HOMO–1, and degenerate LUMO.[43,44] Because of the near-degeneracy of the a_{2u} orbital as the HOMO and the a_{1u} orbital as the HOMO–1 (or the next HOMO of the porphyrin ligand in the case that central-metal-based molecular orbitals (MOs) are inserted in between), transitions from these occupied orbitals to the degenerate LUMO (e_g orbitals) cause configurational interactions to form allowed and forbidden excited states, which correspond to the Soret and Q bands, respectively (Figure 4(a)).

Figure 3 also shows the absorption spectrum of a nickel complex of phthalocyanine (NiPc), which is a tetraazaporphyrin derivative bearing imino nitrogen atoms at the *meso*-positions instead of methine carbon atoms. In contrast to the weak Q band and intense Soret band of porphyrin, Pc normally exhibits intense Q band and a rather broad, featureless Soret band. Gouterman's four orbital theory also explains the difference in the absorption spectral profiles between porphyrin and Pc.

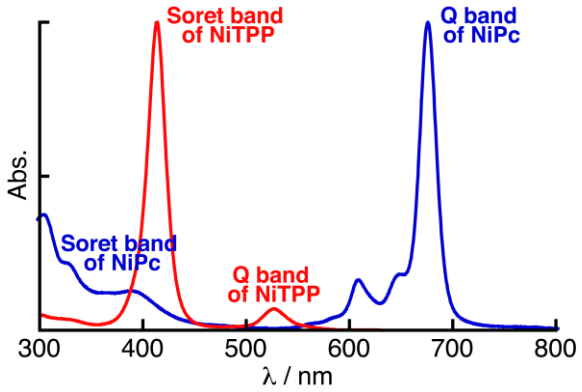

Figure 3. UV/vis absorption spectra of porphyrin and Pc (nickel complexes of *meso*-tetraphenyl-substituted porphyrin (**NiTPP** (red)) and tetra-*tert*-butyl-substituted phthalocyanine (**NiPc** (blue)) in $CHCl_3$

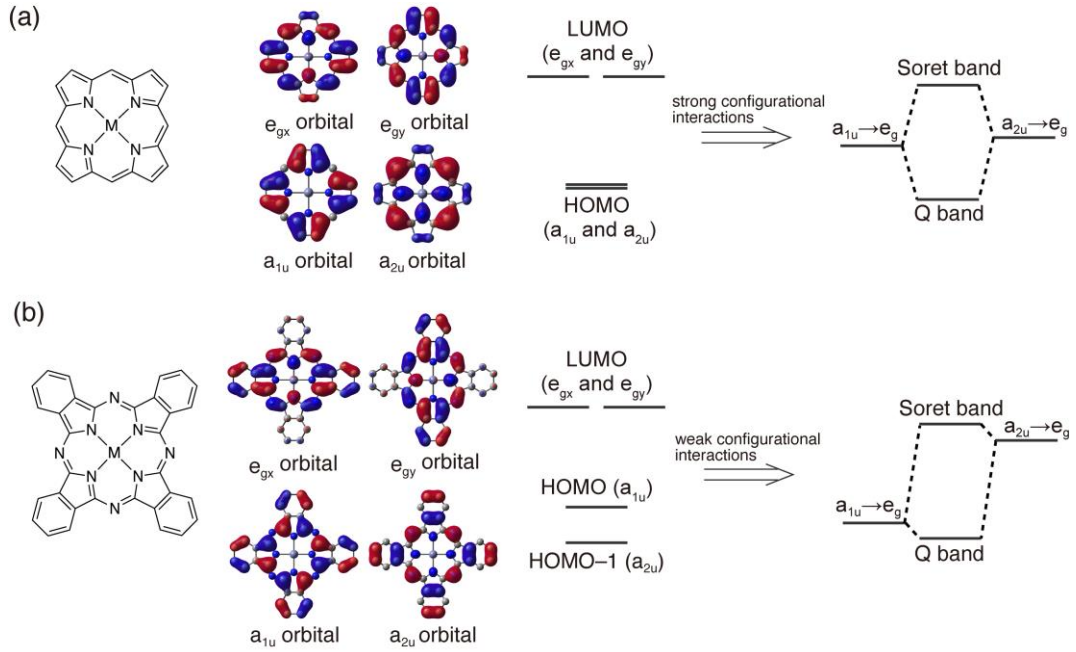

Figure 4. Frontier molecular orbital diagrams of (a) porphyrin and (b) Pc and configurational interactions

In the case of Pc, because of the higher electronegativity of nitrogen than carbon, the a_{2u} orbital having large molecular orbital coefficients on the *meso*-positions is selectively stabilized relative to the a_{1u} orbital. The resulting lifted degeneracy of the a_{1u} orbital as the HOMO and the a_{2u} orbital as the HOMO–1 weakens the configurational interactions. Due to the small configurational interactions, the Q band of Pc gains intensity compared with that of porphyrin. Meanwhile, the Soret bands of Pc are generally broad due to mixing with other transitions such as n-π* bands.

2-2. MCD spectroscopy and Michl's perimeter model in porphyrin chemistry

MCD spectroscopy gives an information about the electronic structures of porphyrin and related analogues, which is complementary to the information provided by UV/vis absorption spectroscopy.[45–48]

MCD spectra are measured by mounting a magnet into a sample compartment of a normal circular dichroism (CD) spectrometer. Because MCD spectroscopy studies difference in absorption between left-handed circularly polarized light (*lcp*) and right-handed one (*rcp*) under magnetic fields known as Faraday effect, MCD signal intensities (ΔA_{l-r}: differential absorbance of *lcp* and *rcp*) relate to the transition magnetic dipole moments. Unlike CD spectroscopy, an MCD signal can be observed even when a molecule lacks chirality and provides information about degeneracy of both ground and excited states, which is essential to understand electronic structures of porphyrin and related analogues.

An MCD spectrum is characterized by three spectral features called Faraday *A*, *B*, and *C* terms. The Faraday *A* term arises from the Zeeman splitting of a *degenerate transition* under a magnetic field, whereas the Faraday *B* term is generated by the field-induced mixing of *nondegenerate transitions* as a second order effect. The Faraday *C* term arises from the Boltzmann population distribution across the degenerate ground state, and the intensity shows temperature dependence. Due to the near- or non-degeneracy of the ground state, Faraday *A* and *B* terms dominate in the MCD spectra of porphyrin and related analogues. As shown in Figure 5, the Faraday *A* term is a derivative-shaped signal corresponding to the absorption band with an inflection point at the absorption maximum, whereas the Faraday *B* term is a gaussian-shaped signal with a similar spectral profile to that of absorption, irrespective of its sign.

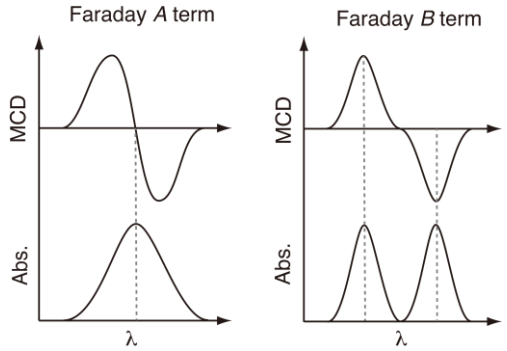

Figure 5. MCD Faraday *A* and *B* terms

In 1970s, Michl developed a general theory to explain the relationship between the magnitude of the frontier orbital splitting energies of aromatic π-systems, *Δ*HOMO and *Δ*LUMO, and the MCD sign sequence based on a [4N+2]-perimeter model.[49–51] *Δ*HOMO and *Δ*LUMO denote the energy gap between the HOMO and HOMO–1 and that between the LUMO and LUMO+1, respectively. In Michl's perimeter model, a π-molecular orbital (π-MO) of the simplified cyclic polyene represents a parent conjugated system for the molecule of interest. The parent [4N+2]-perimeter of porphyrin is a 16-atom 18π-electron $C_{16}H_{16}^{2-}$ π-system. Although a D_{16h} symmetry of the perimeter is modified to a D_{4h} or lower symmetries

in the case of porphyrin and related analogues, nodal patterns of the four frontier orbitals are retained. Figure 6 shows a stack of π-MOs and diagramatic plots of magnetic moments. For each set of degenerate wavefunctions (Ψ_N and Ψ_{-N}), the Ψ_N MO involves electron circulation in an anticlockwise direction, whereas the Ψ_{-N} MO involves that in a clockwise direction. In the transitions, $\Psi_N \rightarrow \Psi_{N+1}$ and $\Psi_{-N} \rightarrow \Psi_{-(N+1)}$, the sense of circulation of excited electron is preserved. In the ground state, the magnetic moment due to the electron circulation of the Ψ_N MO is completely canceled by the magnetic moment caused by the opposite electron circulation of the Ψ_{-N} MO. In contrast, the net circulation of the one-electron excited state, in which the promoted electron is in Ψ_{N+1}, can be different from that of the ground state. Therefore, cancelation of the magnetic moment by the electron remained in Ψ_{-N} is no longer perfect. If the net circulation in the excited state is larger than the ground state, *lcp* absorption causes an anticlockwise loop of current, whereas *rcp* absorption causes a clockwise loop of current. When the net circulation in the excited state is smaller, this relationship becomes opposite due to the dominant contribution of the positive hole left in the Ψ_N to the net circulation. In either case, the circulation of electron produces a magnetic moment referred to as μ^-, which interacts with the magnetic fields due to the Zeeman effect as with ESR and NMR spectroscopies. If μ^- is negative, the energy states excited by *rcp* is a little lower than that excited by *lcp* under the magnetic field, resulting in the minus-to-plus sign sequence in ascending energy. If μ^- is positive, the sign sequence becomes opposite. In addition to the $\Psi_N \rightarrow \Psi_{N+1}$ and $\Psi_{-N} \rightarrow \Psi_{-(N+1)}$ transitions, there are two other HOMO → LUMO transitions, $\Psi_N \rightarrow \Psi_{-(N+1)}$ and $\Psi_{-N} \rightarrow \Psi_{N+1}$, which produces the magnetic moment denoted as μ^+.

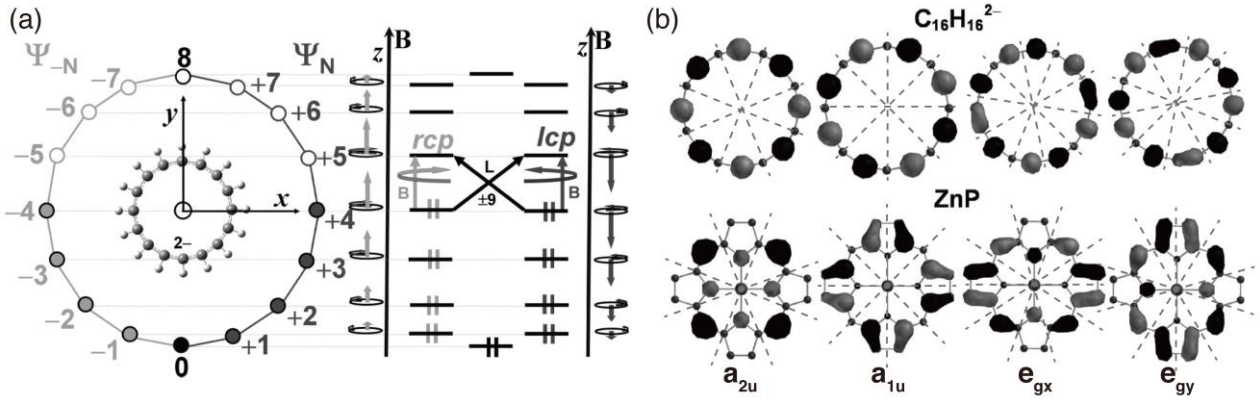

Figure 6. (a) Michl's perimeter model for the $C_{16}H_{16}^{2-}$ parent perimeter of porphyrin and related analogues. For each π-MO, the *z* component of the total orbital angular quantum number is given, and the sense and amount of electron circulation and the direction and magnitude of the resulting magnetic moments predicted based on the LCAO calculations are shown. (b) Frontier MOs for the $C_{16}H_{16}^{2-}$ perimeter and zinc complex of porphin (**ZnP**) predicted by the DFT calculations at the B3LYP/6-31G(d) level. Arbitrary nodal planes are shown with dashed lines. Redrawn from ref. 48.

In the actual molecule of interest, configuration of these four transitions is considered to predict the MCD sign sequence. Because a degree of configuration depends on energy splitting (*Δ*HOMO and *Δ*LUMO) of the frontier orbitals (nearly degenerate HOMO and HOMO–1 and degenerate LUMO) derived from the degenerate HOMO and LUMO of the $C_{16}H_{16}^{2-}$ parent perimeter, the MCD sign sequence is determined by the relative magnitude of *Δ*HOMO and *Δ*LUMO. When *Δ*HOMO > *Δ*LUMO, which is normally the case with porphyrin and related analogues, a minus-to-plus Faraday *A* term or coupled Faraday *B* terms in ascending energy is observed for the Soret and Q bands, whereas the sign sequence becomes opposite (plus-to-minus in ascending energy) in the case of *Δ*LUMO > *Δ*HOMO.

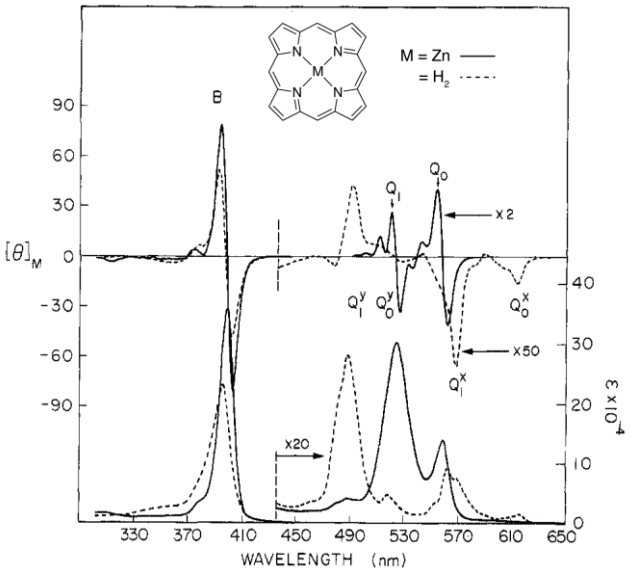

Figure 7. UV/vis absorption (bottom) and MCD (top) spectra of porphin and its zinc complex, and the chemical structure (inset). Redrawn from ref. 52.

Figure 7 shows the UV/vis absorption and MCD spectra of porphin (unsubstituted porphyrin) and its zinc complex as a typical example.[52] In this figure, the Soret band is denoted as a B band. Due to the fourfold molecular symmetry, zinc porphin possesses nearly degenerate HOMO and HOMO–1 and degenerate LUMO. As described in the former section, a forbidden Q band around 560 nm with its vibronic band around 530 nm and an intense Soret band appear in the visible region. Corresponding to these Soret and Q bands, Faraday *A* terms with minus-to-plus sign sequence in ascending energy are observed in the MCD spectrum (Figure 7). The inflection points of these Faraday *A* terms reside at the absorption maxima. In contrast, the absorption spectrum of the free base porphin exhibits four bands in the Q band region. Due to the lower molecular symmetry caused by two amino-pyrroles and two imino-pyrroles, the near-degeneracy of HOMO and HOMO–1 in the case of zinc porphin is lifted, resulting in the split Q bands around 610 and 510 nm (Q_0^x and Q_0^y), which are followed by their vibronic bands around 550 and 490 nm (Q_1^x and Q_1^y). Corresponding to the split Q bands, the Faraday *B* terms with minus-to-plus sign

sequence appear in the MCD spectrum. In the Soret band region, the Faraday *B* terms look like a Faraday *A* term. This kind of MCD signal is called a pseudo Faraday *A* term, which is observed when molecules with less than threefold molecular symmetry possess non-degenerate excited states with accidentally small energy differences.[53]

As shown in Figure 8, the UV/vis/NIR absorption spectra of antiaromatic porphyrin analogues are different from those of aromatic porphyrin analogues, exhibiting a broad, ill-defined band ranging from the visible to NIR regions and several moderately intense bands in the visible region. In Figure 8a, the UV/vis/NIR absorption and MCD spectra of bis-gold(III) complex of antiaromatic [28]hexaphyrin (**Au$_2$[28]Hexa**) are shown.[54] Hexaphyrin is a ring-expanded porphyrin analogue consisting of six pyrrole rings and six bridging methine carbon atoms.[55,56] Because of the expanded macrocyclic structure, hexaphyrin can take interconvertible 26π-electron and 28π-electron redox states (**Au$_2$[26]Hexa** and **Au$_2$[28]Hexa** in Figure 8b): the number in the square bracket before the compound name indicates the number of π-electrons involved in the main conjugation.

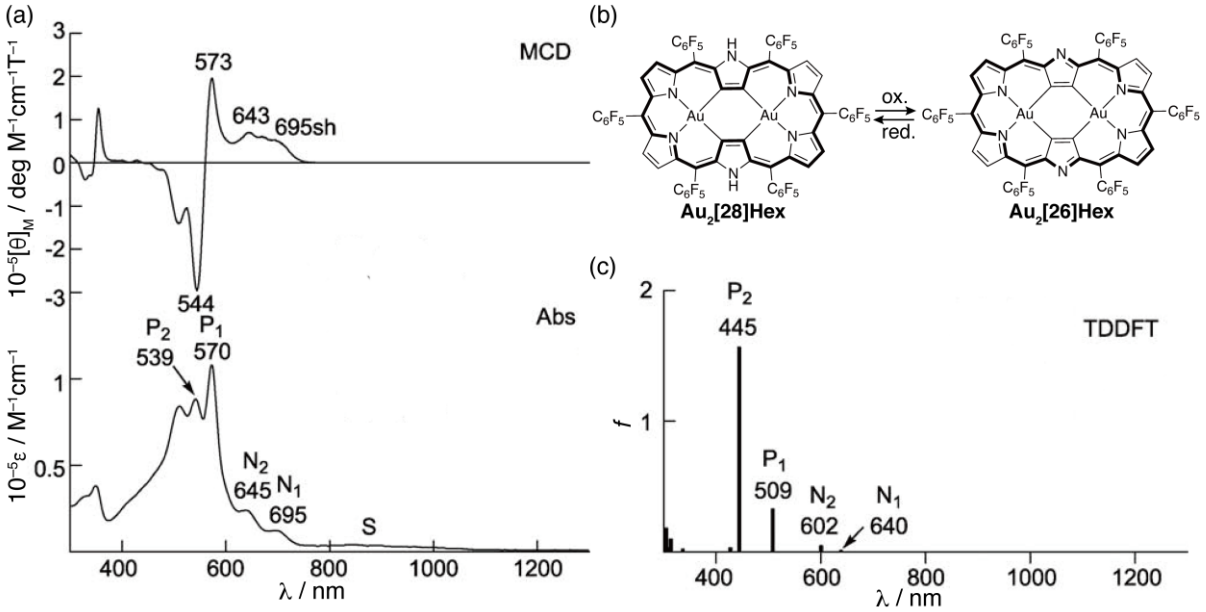

Figure 8. (a) UV/vis/NIR absorption (bottom) and MCD (top) spectra of **Au$_2$[28]Hexa** in CH_2Cl_2. (b) Chemical structures of **Au$_2$[28]Hexa** (left) and **Au$_2$[26]Hexa** (right) and their redox interconversion. The main conjugation pathways are highlighted with bold lines. (c) The calculated stick absorption spectrum of **Au$_2$[28]Hexa** based on the TDDFT calculation at the B3LYP/LanL2DZ level. Redrawn from ref. 54.

To explain the UV/vis/NIR absorption and MCD spectra of antiaromatic compounds, Michl *et al.* developed a [4N]-perimeter model instead of the [4N+2]-perimeter for aromatic compounds.[57–59] In this model, six frontier orbitals, *h*–, *h*+, *s*–, *s*+, *l*–, and *l*+, derived by a symmetry perturbation of the HOMO, singly occupied molecular orbital (SOMO), and LUMO of the [4N]-perimeter contribute to the main transitions referred to as S, N (N_1 and N_2), and P (P_1 and P_2) bands. The lowest-energy S band arises from

s– → *s*+ transition. Because of the intrashell nature of this transition, the S band is electric dipole forbidden so that the absorption and MCD intensities of the S band are predicted to be zero. In contrast, the N and P bands are electric dipole allowed and observed as weak and intense bands, respectively. The relationship of the N and P bands is similar to that of the Soret and Q bands for aromatic porphyrin analogues. The N_1 and P_1 bands and N_2 and P_2 bands arise from the configurational interactions of *s*– → *l*– and *h*+ → *s*+ transitions and *s*– → *l*+ and *h*– → *s*+ transitions, respectively. Cancelation and intensification of the transition dipole moments causes weak N_1 and N_2 bands and intense P_1 and P_2 bands. As with the MCD sign sequences of the Soret and Q bands of aromatic porphyrin and related analogues, those of the N and P bands are also dictated by the energy differences, *ΔHL*, *ΣHL*, and *ΔHSL*, defined using frontier orbital energies, *E*(*h*–), *E*(*h*+), *E*(*s*–), *E*(*s*+), *E*(*l*–), and *E*(*l*+): *ΔHSL* = 2(*ΔHS* – *ΔSL*), *ΔHL* = *ΔH* – *ΔL*, and *ΣHL* = *ΔH* + *ΔL* where *ΔH* = *E*(*h*+) – *E*(*h*–), *ΔL* = *E*(*l*+) – *E*(*l*–), *ΔHS* = [*E*(*s*+) + *E*(*s*–)]/2 – [*E*(*h*+) + *E*(*h*–)]/2, *ΔSL* = [*E*(*l*+) + *E*(*l*–)]/2 – [*E*(*s*+) + *E*(*s*–)]/2.

Michl's [4N]-perimeter model can be suitably applied to analyze the UV/vis/NIR absorption and MCD spectra of **Au_2[28]Hexa** (Figures 8 and 9). The weak, ill-defined band without any MCD signals ranging in the NIR region was assigned to the S band, whereas the following two weak and two intense bands were ascribed to the N and P bands, respectively. Although the MCD sign sequence was not discussed in detail, it was reported that the coupling between the *h*+ → *s*+ transition in P_1 band and *h*– → *s*+ transition in P_2 band must be dominant for the MCD signals of **Au_2[28]Hexa** considering the plus-to-minus sign sequence was observed for the P bands.

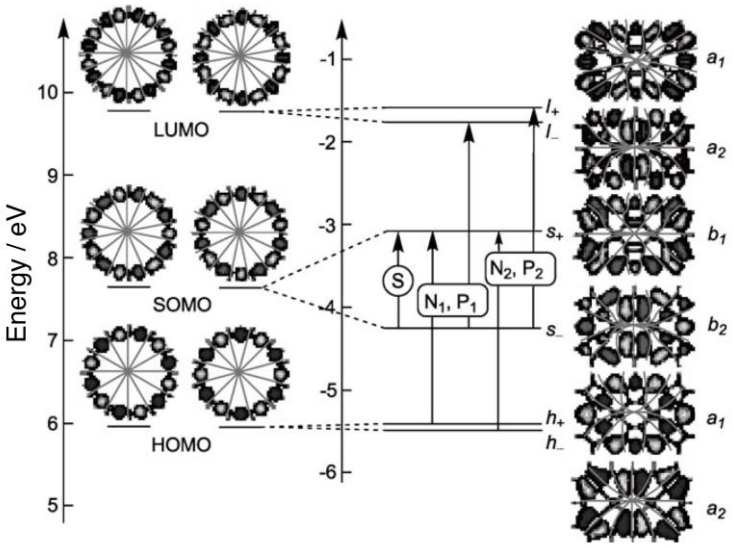

Figure 9. Frontier molecular orbital diagram of **Au_2[28]Hexa** and its 24-atom 28π-electron $C_{24}H_{24}^{4-}$ perimeter (B3LYP/LanL2DZ). Arbitrary nodal planes are drawn with gray lines. Redrawn from ref. 54.

3. 5,15-DIHETEROPORPHYRINS

3-1. 5,15-Diaminoporphyrin

5,15-Diaminoporphyrin formally possesses a 20π-electron antiaromatic conjugated system due to incorporation of the lone pair electrons of *meso*-amino nitrogen atoms into the π-conjugation of porphyrin. In 2016, Shinokubo and Matano independently synthesized this antiaromatic 5,15-diheteroporphrin by different methods.[60–62] Shinokubo *et al.* found that conversion of nickel(II) complex of 5,15-diazaporphyrin **1** into *N*,*N*′-unsubstituted 5,15-diaminoporphyrin **2** proceeded quantitatively upon reduction with *N*,*N*′-bis(trimethylsilyl)-1,4-dihydropyrazine, and **2** was obtained in 84% yield after treatment of the resulting solution with an excess amount of methanol (Scheme 8). A free base **4** was similarly synthesized from **3** in 78% yield. **2** and **4** were air-sensitive and readily oxidized back to 5,15-diazaporphyrins in solution by exposure to air.

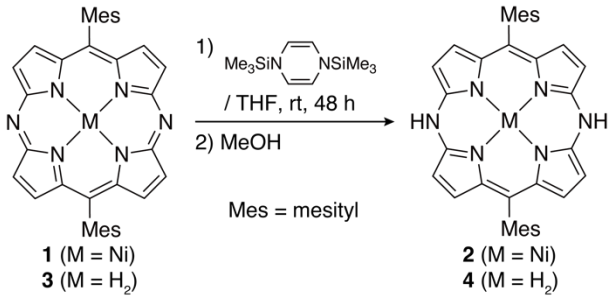

Scheme 8. Synthesis of *N*,*N*′-unsubstituted 5,15-diaminoporphyrin (**2** and **4**)

The crystal structures of **2** and **4** are highly planar with small mean plane deviations (< 0.05 Å) (Figure 10). As a diagnostic feature of antiaromatic porphyrin analogues, bond-length alternations were also observed.

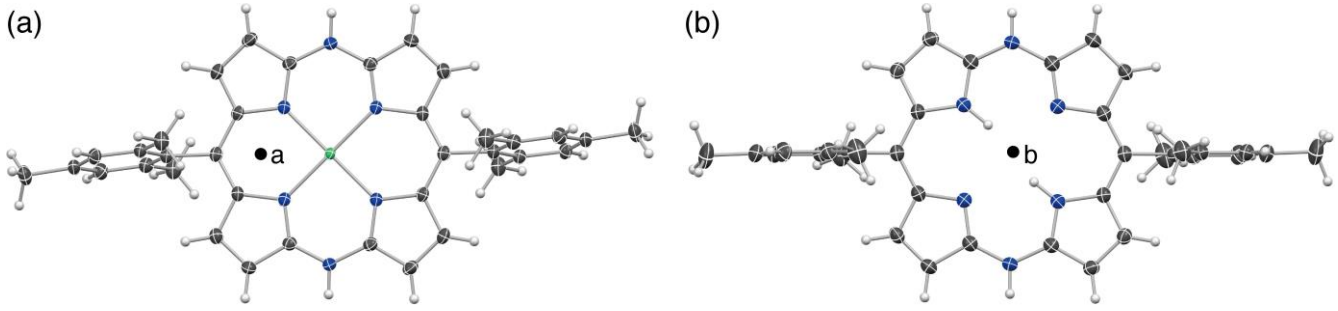

Figure 10. X-Ray single crystal structures of (a) **2** and (b) **4**. The thermal ellipsoids are scaled to the 50% probability level.

The strong paratropic ring current effect arising from the 20π-antiaromaticity of 5,15-diaminoporphyrin was both experimentally and theoretically confirmed. The nucleus-independent chemical shift (NICS) values are largely positive, +15.5 and +15.8 ppm at the "a" and "b" positions in Figure 10, respectively. In

the ^{1}H NMR spectra, the β-proton signals were upfield shifted (δ = 3.0–4.5 ppm), whereas the inner NH protons of **4** were observed in the downfield region at δ = 24.5 ppm. In analogy with porphyrins, **4** exhibited the inner NH tautomerism, but its activation energy of 14.3 kcal mol^{-1} at 25 ºC was substantially higher than that of typical porphyrins (ca. 12 kcal mol^{-1}).

N,*N*′-Unsubstituted 5,15-diaminoporphyrin (**7** and **8**) was accidentally formed as a by-product of the sulfonylation reaction of a mixture of 3,13- and 3,17-dibromo-5,15-diazaporphyrins (**5** and **6**) (Scheme 9).[61] The corresponding 3,7,13,17-tetrasulfonyl-5,15-diazaporphyrin (**9** and **10**) was also obtained as a main product of this reaction. Unlike the unsubstituted 5,15-diaminoporphyrin (**2** and **4**), **7** and **8** were stable due to the presence of the electron-withdrawing sulfonyl groups. Despite the downfield shifts of the β-protons and NH-protons from those of **2** by $\Delta\delta$ = 1.5–2.1 ppm and 2.5 ppm, respectively, caused by the adjacent sulfonyl groups, **7** retained a certain degree of antiaromaticity.

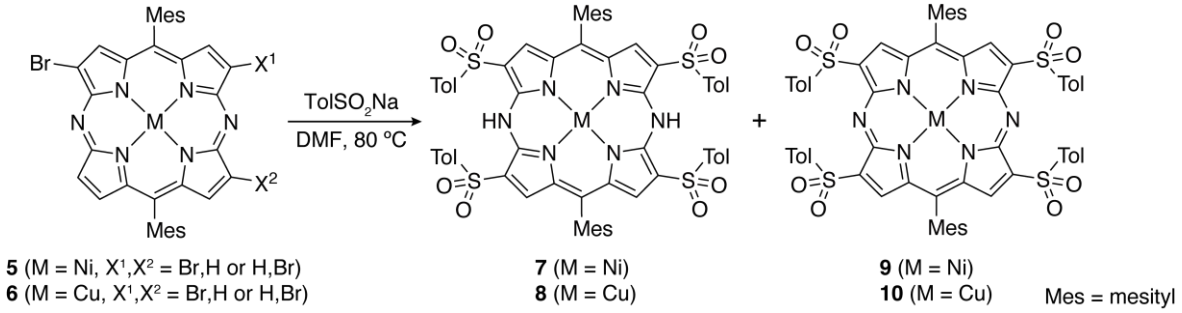

Scheme 9. Synthesis of tetrasulfonyl-*N*,*N*′-unsubstituted 5,15-diaminoporphyrin (**7** and **8**)

Matano *et al.* reported the synthesis of *N*,*N*′-diaryl-substituted 5,15-diaminoporphyrin nickel(II) complex **11** as an air-stable form in a stepwise manner from 1-chloro-9-arylamino-5-mesityldipyrrin via its nickel(II) complex (Scheme 10).[62] The key 1-chloro-9-arylaminodipyrrin precursor was synthesized from a nucleophilic amination reaction of α,α′-dichlorodipyrrin and arylamines. **11** was quantitatively oxidized to its 18π-aromatic dication **12** upon treatment with two equivalents of tris(4-bromophenyl)ammoniumyl hexachloroantimonate (Magic Blue) or silver(I) hexafluorophosphate ($AgPF_6$). The intermediate 19π-radical cation species **13** was also generated by a single electron transfer (SET) from **11b** to **12b-P**. Other metal complexes such as zinc (**14**) and copper (**17**) were also synthesized from 1-chloro-9-arylamino-5-mesityldipyrrin under slightly modified reaction conditions (Scheme 10).[63] In the synthesis of the zinc complexes, the annulation reaction proceeded smoothly when NaO*t*Bu and toluene were used instead of K_2CO_3 and DMF. In the case of the copper complexes, a copper(II) salt promoted not only annulation of the copper(II) dipyrrin complex into 5,15-diaminoporphyrin but also oxidation to the 19π-radical cation species. This radical cation was reduced to the 20π-neutral form (**17**) upon

treatment with $NaBH_4$. The corresponding 18π-aromatic dications (**15** and **18**) were synthesized by oxidation with two equivalents of $AgPF_6$, whereas the 19π-radical cations (**16** and **19**) were generated by reduction of **15** with $NaBH_4$ or bis(cyclopentadienyl)cobalt(II) ($CoCp_2$) and by a SET reaction of **17** and **18**, respectively (Scheme 10). Furthermore, demetallation of the central zinc ion of **14c** in the Yorimitsu–Osuka procedure[64] using a Grignard reagent provided a free base form **20**, which was transformed to its 19π-radical cation **21** and 18π-aromatic dication **22** by stepwise oxidation with an equimolar amount of $AgPF_6$ (Scheme 11).[63]

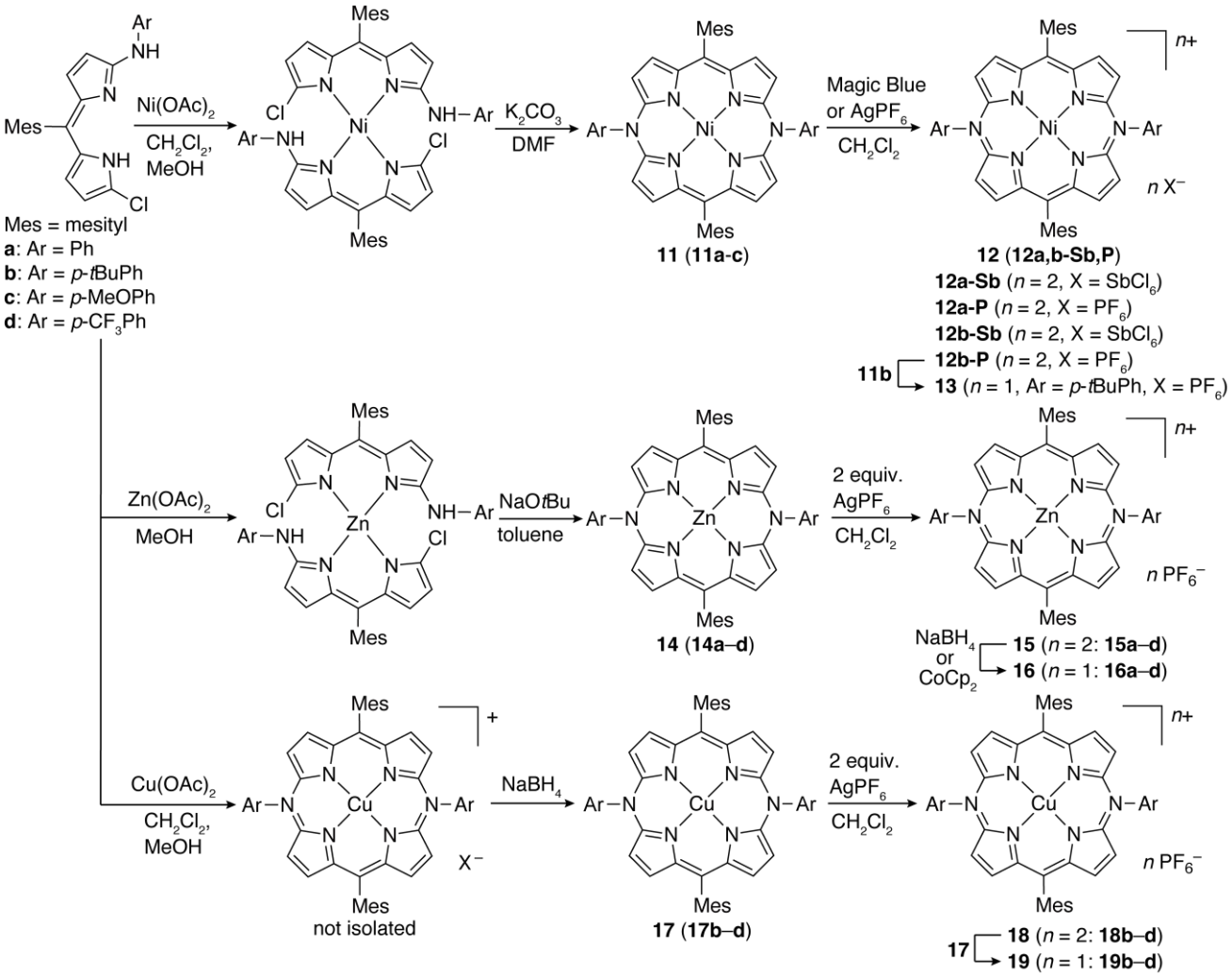

Scheme 10. Synthesis of *N*,*N*′-diaryl-substituted 5,15-diaminoporphyrin (**11**, **14**, and **17**) and transformation to 18π-aromatic dication (**12**, **15**, and **18**) and 19π-radical cation (**13**, **16**, and **19**)

As with the crystal structures of *N*,*N*′-unsubstituted 5,15-diaminoporphyrins, *N*,*N*′-diaryl-substituted 5,15-diaminoporphyrins exhibited planar structures with small root-mean square deviations (< 0.04 Å) in both the 20π-antiaromatic neutral state (**11b**) and 18π-aromatic dication state (**12a-Sb**) (Figure 11). The *N*-aryl groups were almost perpendicular to the 5,15-diaminoporphyrin core, suggesting the minor

substituent effect. The bond lengths between *meso*-nitrogen and α-pyrrolic carbon were shorter than those between *meso*-nitrogen and *ipso*-aryl carbon, implying that the lone pair electrons of the *meso*-nitrogen atoms were included in the macrocyclic conjugated system.

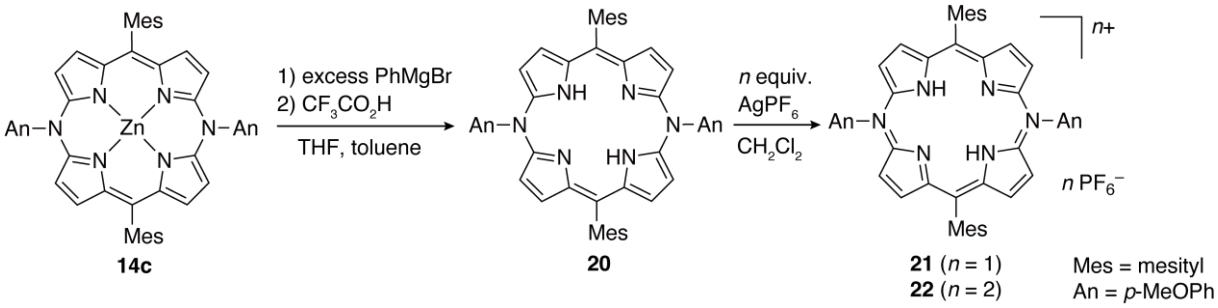

Scheme 11. Demetallation of zinc complex of *N*,*N*′-diaryl-substituted 5,15-diaminoporphyrin **14c** to free base **20** and the stepwise oxidation to 19π-radical cation **21** and 18π-aromatic dication **22**

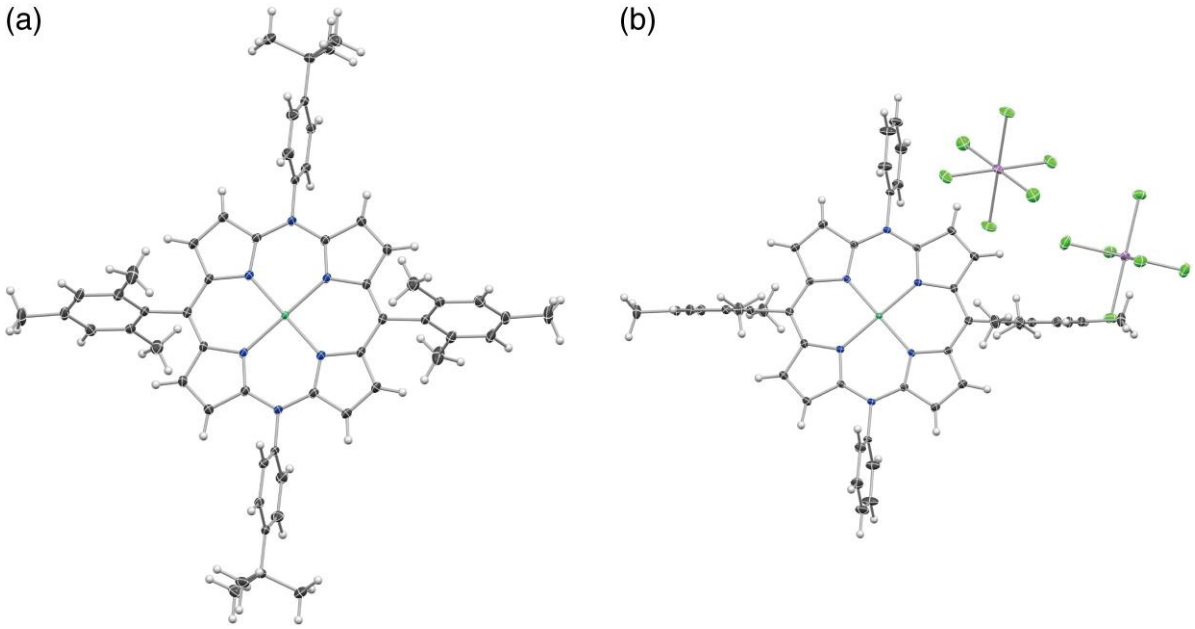

Figure 11. X-Ray single crystal structures of (a) **11b** and (b) **12a-Sb**. The thermal ellipsoids are scaled to the 50% probability level.

In the ^{1}H NMR spectra, the β-pyrrolic protons of **11a** were upfield shifted at δ = 4.61 and 3.30 ppm in C_6D_6, whereas those of **12a-Sb** were detected downfield at δ = 8.72 and 8.33 ppm in CD_2Cl_2 (Figure 12). The inner NH protons of **20** resonated at δ = 24.87 ppm in C_6D_6, whereas **22** exhibited the inner NH signal at δ = –0.54 ppm in $CDCl_3$. These results indicate the paratropic and diatropic ring currents of the 20π-antiaromatic neutral form and 18π-aromatic dication form, respectively. In analogy with the *N*,*N*′-unsubstituted 5,15-diaminoporphyrin (**2** and **4**), the NICS values of a model structure of **14**, in which all the aryl substituents were replaced with phenyl groups, were positive (δ = +8.13 and +9.32 ppm) at the

midpoint between the two adjacent pyrrole rings. Meanwhile, Matano *et al*. pointed out that the negative NICS value at the center of the pyrrole rings (δ = –6.51 ppm) implied the presence of local diatropic ring currents in the pyrrole rings.

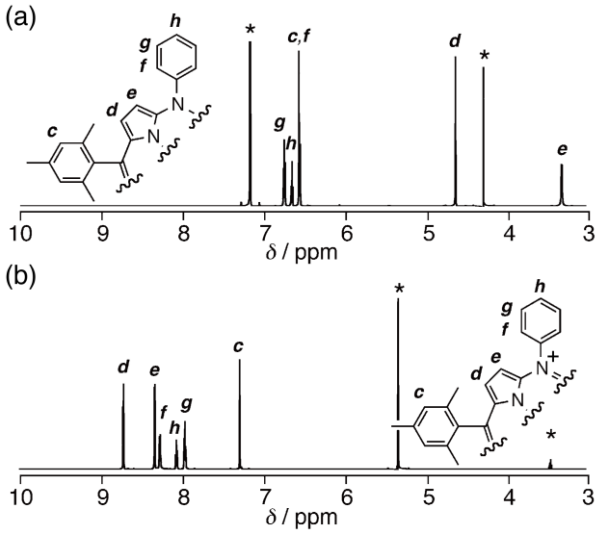

Figure 12. ^{1}H NMR spectra of (a) **11a** in C_6D_6 and (b) **12a-Sb** in CD_2Cl_2. Reprinted with permission from ref. 62 Copyright 2016 Wiley.

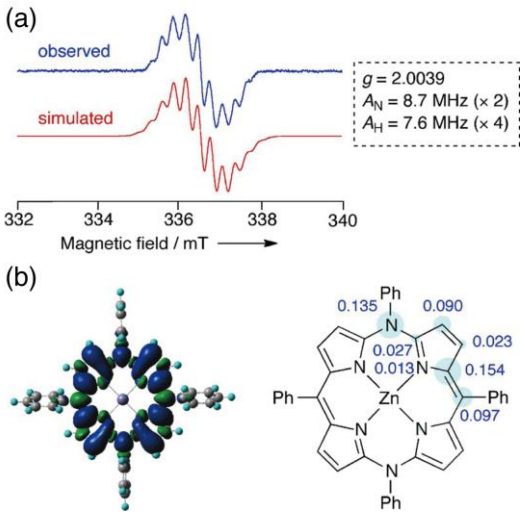

Figure 13. (a) ESR spectra of **16c** observed in toluene (blue) and simulated (red). (b) Spin-density distribution of the optimized structure (left) and spin densities (right) calculated by the DFT method at the B3LYP/6-311G(d,p) level. Reprinted with permission from ref. 63 Copyright 2017 Wiley.

The 19π-radical cations and copper complexes were characterized by ESR spectroscopy. The ESR spectra of the 19π-radical cations of nickel and zinc complexes and the free base forms exhibited a ligand-centered ESR signal at g = 1.9981–2.0039 with fine structures derived from two *meso*-^{14}N and four β-^{1}H atoms, which were supported by the calculated spin distribution (Figure 13).

The absorption spectra of both *N*,*N'*-unsubstituted and *N*,*N'*-diaryl-substituted 5,15-diaminoporphyrin metal complexes (**2**, **11**, **14**, and **17**) exhibited two intense bands with the absorption maxima (λ_{max}) around 525 and 445 nm (Figure 14).[60,62,63] There is a small dependence of the absorption wavelengths on the central metal ions and substituents at the *meso*-nitrogen positions. The slight blue shifts of these intense bands were observed for the free base forms (**4** and **20**), respectively (λ_{max} of **20**: 488 and 426 nm). The weak, forbidden band ranging from 700 to 1200 nm, which is diagnostic of antiaromatic compounds, was reported in the case of *N*,*N'*-unsubstituted 5,15-diaminoporphyrin (**2** and **4**).[60] These absorption spectral features can be characterized on the basis of the Michl's [4N]-perimeter model with the S, N, and P bands (*vide supra*). This assignment was also supported by the TDDFT calculations on the *N*,*N'*-diaryl-substituted 5,15-diaminoporphyrins, which predicted the symmetrically forbidden nature of the HOMO-to-LUMO transition and major contribution of the HOMO-to-LUMO+1 and HOMO–1-to-LUMO transitions to the lower-energy band among the two intense bands. The same numbers of nodal planes for the HOMO–1 and HOMO–2 and for the HOMO and LUMO also reflect the electronic structure delineated with the [4N]-perimeter model (Figure 15).

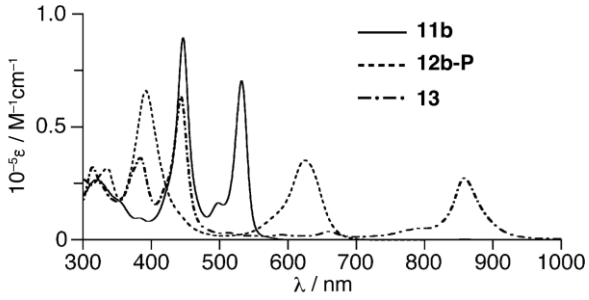

Figure 14. UV/vis/NIR absorption spectra of **11b**, **12b-P**, and **13** in CH_2Cl_2. Redrawn from ref. 62.

Reflecting the aromatic porphyrin-like electronic structure, the dication species (**12**, **15**, and **18**) exhibited intense Soret and Q bands with λ_{max} around 390 and 630 nm, respectively. Due to the lifted degeneracy of the HOMO and HOMO–1 (**15-m** in Figure 15) caused by more electronegative nitrogen than carbon at the *meso*-positions, the Q band gains almost similar intensity to that of the Soret band. The observed absorption spectral difference between the dication species and isoelectronic metalloporphyrins is analogous to that between Pc and porphyrin. Upon removal of two electrons from the conjugated system, the MO distribution patterns and number of nodal planes of the frontier four orbitals become similar to those of **ZnTPP-m**, reflecting the aromatic 18π-electron conjugated system of the dication species. The radical cation species (**13**, **16**, and **19**) exhibited a characteristic NIR band around 880 nm in addition to the two intense bands in the visible region (Figure 14).

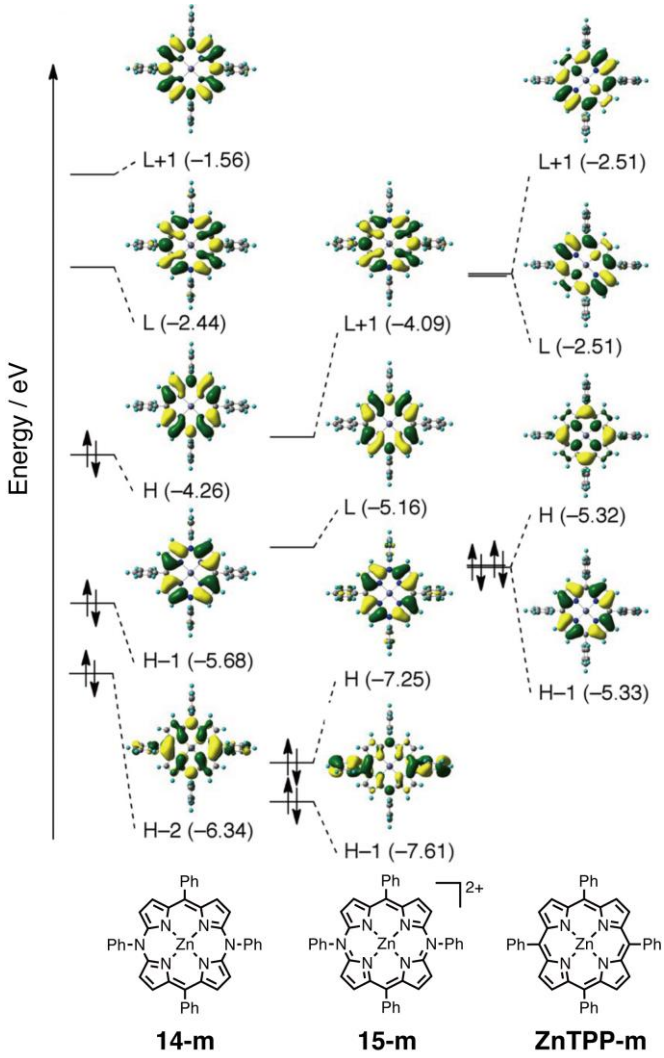

Figure 15. MO diagrams of model structures, **14-m** for **14**, **15-m** for **15**, and **ZnTPP** for *meso*-tetraphenyl-substituted porphyrin zinc(II) complex calculated by the DFT method at the B3LYP/6-311G(d,p) level with the solvent effect (PCM, CH_2Cl_2). Redrawn from ref. 63.

The cyclic voltammograms revealed the two reversible oxidation for *N*,*N'*-diaryl-substituted 5,15-diaminoporphyrin (**11**, **14**, **17**, and **20**) corresponding to the 1-electron oxidation from 20π-electron neutral state to 19π-electron radical cation (20π/19π oxidation) and further to 18π-electron dication (19π/18π oxidation) (Figure 16a). The oxidation potentials both shifted to the negative in the order of free base **20**> nickel complex **11c** > copper complex **17c** > zinc complex **14c** due to the smaller electronegativity of the zinc atom compared with other metal atoms. The small but distinct effects of the *para* substituents of the *N*-aryl groups on the oxidation potentials were observed for a series of zinc complexes (**14a**–**d**): the electron-donating methoxy and *tert*-butyl groups caused slight negative shifts, whereas the electron-withdrawing trifluoromethyl group shifted them to more positive potentials (Figure 16b).

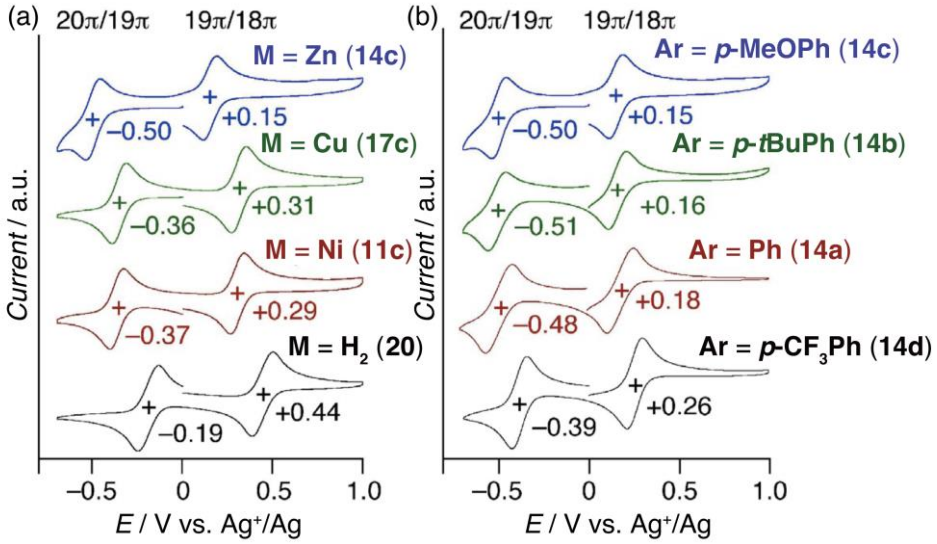

Figure 16. Cyclic voltammograms of (a) *N*,*N*′-diaryl-substituted 5,15-diaminoporphyrin bearing *N*-*p*-anisyl groups (M = Zn, Cu, Ni, and H_2) and (b) zinc complexes bearing different *para* substituents of the *N*-aryl groups (**14a**–**d**) in CH_2Cl_2 containing 0.1 M Bu_4NPF_6 as a supporting electrolyte at a scan rate of 60 mV s^{-1}. Redrawn from ref. 63.

The substituent effect has been further investigated by introducing electron-donating *p*-tertiary-aminophenyl groups as an *N*-aryl substituent (Figure 17a).[65] In addition to the diagnostic absorption spectral profiles of the neutral, radical cation, and dication forms, the dication species of **23** and **24** exhibited additional broad absorption in the NIR region (700–1200 nm). On the basis of the TDDFT calculations and comparison of the absorption spectra with other dication species (**12** and **18**), this new band was assigned as a charge transfer band from the tertiary amine as a donor to 5,15-diazaporphyrin core as an acceptor. In addition to two reversible redox couples, which correspond to the 20π/19π and 19π/18π redox reactions, both **23** and **24** exhibited irreversible oxidation processes at more positive potentials due to the oxidation of amine moieties. The repeat CV scans for **23b** between –0.47 to +1.03 V *vs*. Fc^+/Fc with freshly polished working electrodes revealed generation of a new pair of peaks from the first cathodic scan and increase of both cathodic and anodic peak currents (Figure 17b). The observed electrochemical behavior can be ascribed to ammoniumyl radical-mediated formation of benzidine-linked polymers on the electrode surface.

During demetallation of **14c** using a Grignard reagent (PhMgBr), Matano *et al*. noticed **14c** was first transformed into its magnesium complex **25**, which was extremely sensitive to air and easily oxidized to its 19π-radical cation form in air. This reactivity motivated them to use **25** as a redox-active catalyst for an oxidative homocoupling of PhMgBr in the presence of molecular oxygen (Scheme 12). The reaction progress monitored by the ^{1}H NMR and ESR spectra revealed the formation of biphenyl and the 19π-radical cation and clearly demonstrated the catalytic cycle of **25**. Using this catalytic cycle, the

oxidative homocoupling of 2-naphthylmagnesium bromide in the presence of 1 mol% of **14c** in THF was conducted to obtain 2,2'-binaphthyl in 31% yield after 6 h with the catalytic turnover number of 31.[63]

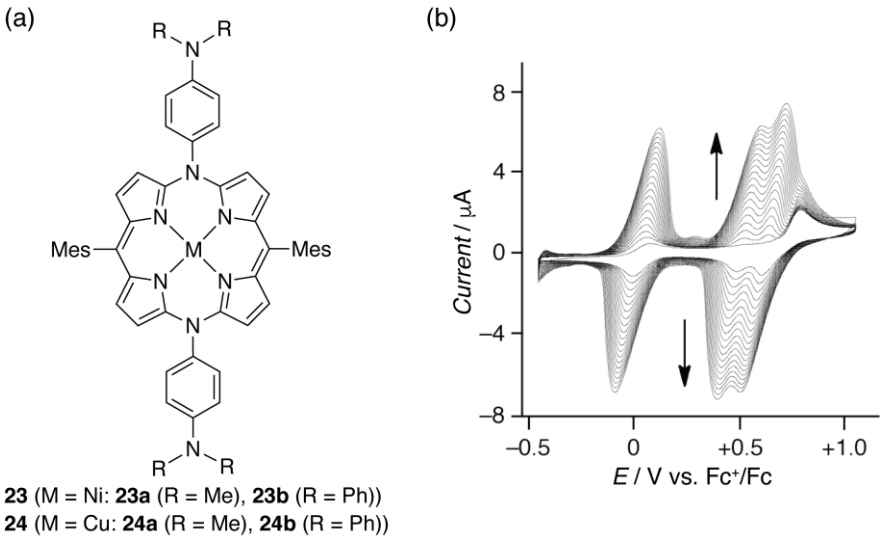

Figure 17. (a) Chemical structure of 5,15-diamionoporphyrins bearing tertiary aminophenyl groups and (b) cyclic voltammograms of **23b** in CH_2Cl_2 with 0.1 M Bu_4NPF_6 as a supporting electrolyte. Repetitive scans (20 times) in the range of –0.47 to +1.03 V *vs.* Fc^+/Fc at a scan rate of 20 mV s^{-1}. Redrawn from ref. 65.

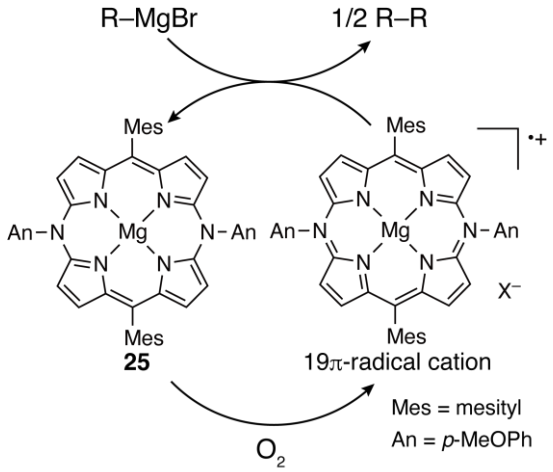

Scheme 12. Plausible catalytic cycle for the magnesium complex-catalyzed oxidative homocoupling reaction

3-2. 5-Amino-15-azaporphyrin

Matano *et al*. synthesized 5-amino-15-azaporphyrin under similar reaction conditions to those of 5,15-diaminoporphyrin using an asymmetric bis(dipyrrin) nickel(II) complex bearing *N*-benzylamino and *N*-arylamino groups (Scheme 13).[66] When potassium carbonate and DMF were used (method A in Scheme 13), elimination of the *N*-benzyl group occurred during the annulation, and 5-amino-15-azaporphyrin **26** was obtained as a neutral 19π-radical form. **26** was oxidized to a cation form

(**27**) for isolation, and **26** was obtained as a pure form by reducing **27** with $CoCp_2$. When NaO*t*-Bu and toluene were used instead of potassium carbonate and DMF, *N*-benzyl group remained intact, and a 5,15-diaminoporphyrin dication bearing *N*-benzyl group (**28**) was obtained after treating the reaction mixture with $AgPF_6$. The *N*-benzyl group was cleaved by exposing to dihydrogen gas in the presence of Pd/C to provide a putative 20π-electron conjugated species, which was further oxidized to 5-amino-15-azaporphyrin with $AgPF_6$. This two-step method (method B in Scheme 13) was effective for the synthesis of **27d** with an electron-withdrawing *p*-trifluoromethylphenyl substituent.

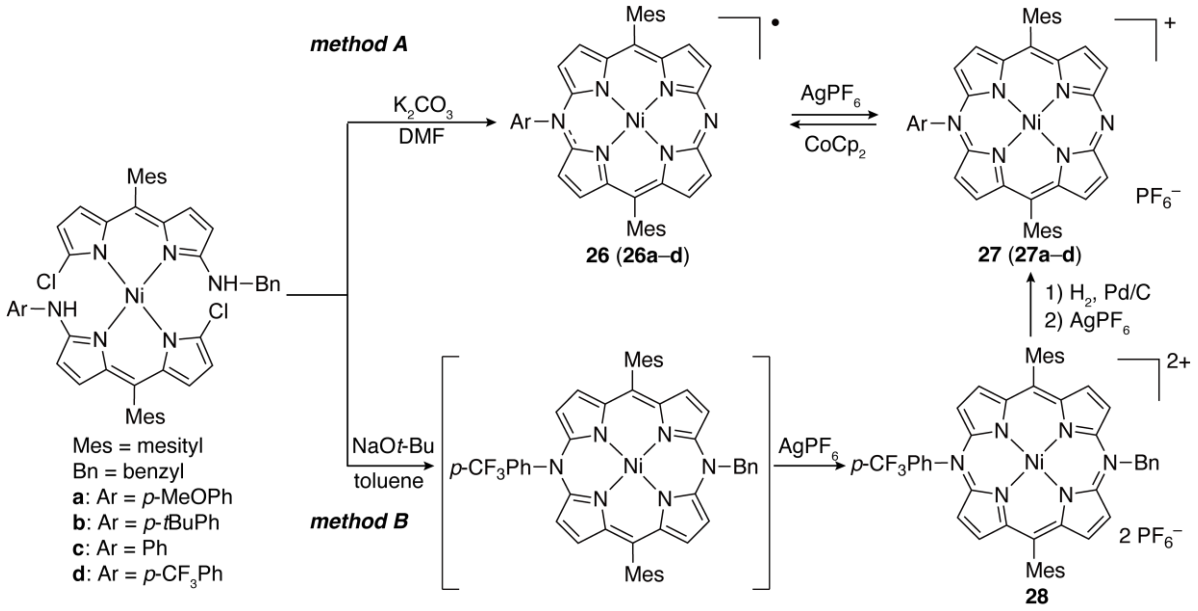

Scheme 13. Synthesis of 5-amino-15-azaporphyrin **26** and monocation **27**

In analogy with the *N*,*N*′-diaryl-substituted 5,15-diaminoporphyrin dication, **27** exhibited β-proton signals at δ = 9.22–8.38 ppm, which fall between those of 5,15-diazaporphyrin and *N*,*N*′-diaryl-substituted 5,15-diaminoporphyrin dication. This result revealed the aromatic character of **27** as well as the impact of the net charge on the shielding effects. In the absorption spectra of **27**, the red-shift of the Q band was observed compared with *N*,*N*′-diaryl-substituted 5,15-diaminoporphyrin dication bearing the same substituents due to the slightly smaller HOMO–LUMO gap. Cyclic voltammetry revealed three reversible redox processes in the ranges –1.02 to –0.85 V, –0.39 to –0.32 V, and +1.41 to +1.47 V (*vs.* Ag^+/Ag), which correspond to 20π/19π, 19π/18π, and 18π/17π redox processes (Figure 18a). These redox potentials, which resided between those of the corresponding *N*,*N*′-diaryl-substituted 5,15-diaminoporphyrin dication and 5,15-diazaporphyrin demonstrated the impact of the net charges on the 18π-conjugated system (Figure 18b). The positive shift of the 19π/18π redox potential from that of 5,15-diazaporphyrin also explained the high air-stability of the neutral radical species (**26**).

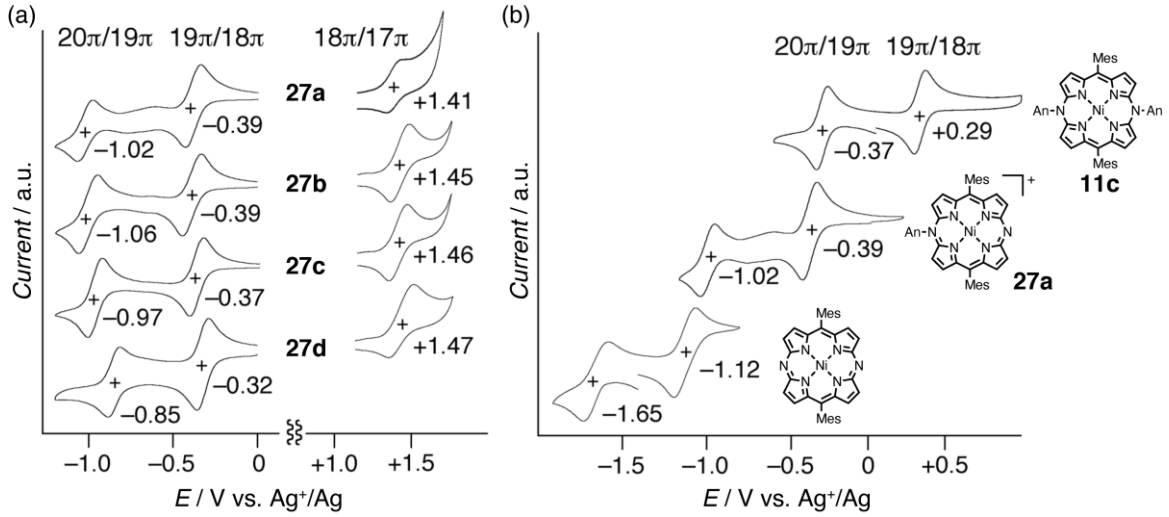

Figure 18. Cyclic voltammograms of (a) 5-amino-15-azaporphyrin monocations **27a**–**d** and (b) **27a**, *N*,*N'*-diaryl-substituted 5,15-diaminoporphyrin **11c**, and 5,15-diazaporphyrin in CH_2Cl_2 containing 0.1 M Bu_4NPF_6 as a supporting electrolyte at a scan rate of 60 mV s^{-1}. Redrawn from ref. 66.

3-3. 5,15-Dioxaporphyrin

As with 5,15-diaminoporphyrin, introduction of two chalcogen atoms, such as oxygen and sulfur, at the *meso*-positions can generate 20π-antiaromatic conjugated systems. Among such chalcogen-atom-containing heteroporphyrins, the antiaromatic characters of 5,15-dioxaporphyrin have been revealed. We have recently developed a rational synthesis of 5,15-dioxaporphyrin **29** by a nucleophilic substitution reaction of a bis(α,α'-dibromodipyrrin) nickel(II) complex with benzaldoxime followed by an *in situ* annulation of the α-hydroxy-substituted intermediate (Scheme 14).[67]

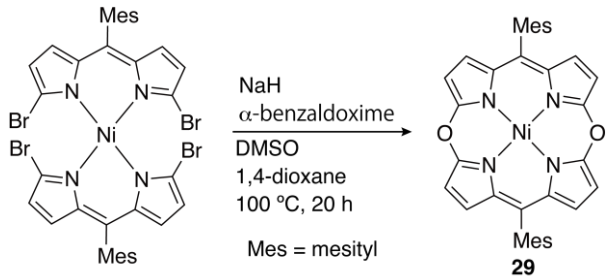

Scheme 14. Synthesis of 5,15-dioxaporphyrin **29**

The crystal structure of **29** exhibited a planar structure with a small root-mean-square deviation < 0.08 Å and shorter C–O bond lengths of 1.34–1.35 Å than a typical C(sp^2)–O bond of ca. 1.40 Å (Figure 19). Because of the planar structure with 20π-electron conjugation, **29** is antiaromatic according to the Hückel rule for aromaticity. In the ^{1}H NMR spectrum, β-proton signals were resonated at δ = 5.66 and 5.12 ppm, which were upfield shifted from that of normal pyrrole at δ = 6.2 ppm. However, the downfield shifts from those of 5,15-diaminoporphyrin at δ = 4.7–2.8 ppm indicated the weak paratropic ring current effect

of **29**, which can be generalized in terms of the smaller diatropicity of furan than pyrrole due to the greater electronegativity of oxygen than nitrogen.

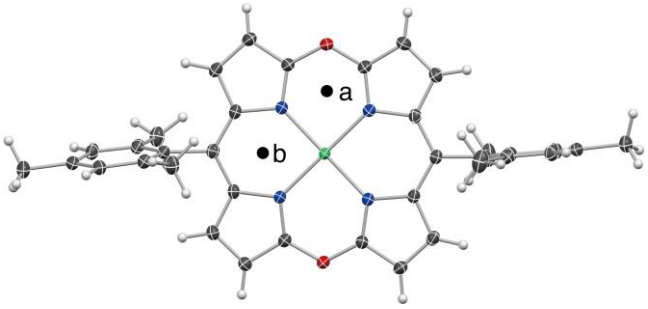

Figure 19. X-Ray single crystal structure of 5,15-dioxaporphyrin **29**. The thermal ellipsoids are scaled to the 50% probability level.

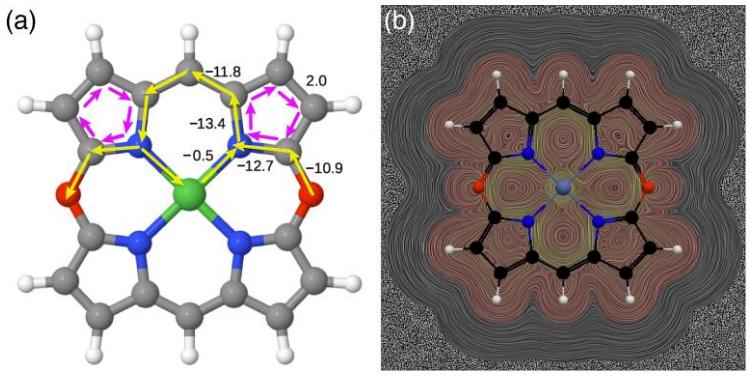

Figure 20. (a) Integrated total current strength susceptibility values for the selected bonds in nA/T. Yellow and violet arrows indicate paratropic and diatropic ring currents. (b) Streamline visualization of the magnetically induced current density in a plane placed 1 Bohr below the molecular plane. Reprinted with permission from ref. 67 Copyright 2018 Wiley.

The positive NICS(0) values of **29** at the "a" and "b" positions designated in Figure 19 (δ = +6.9 and +8.1 ppm for a and b, respectively) also supported the smaller paratropicity than 5,15-diaminoporphyrin, which exhibits NICS(0) values of δ = +14.5 and +15.5 ppm at the same position in the structure of **2**.[60] In analogy with 5,15-diaminoporphyrin, the negative NICS(0) values at the centers of pyrrole rings (δ = –3.9 ppm) implied local diatropic ring current in the pyrrole rings. The GIMIC[41,42] calculation further quantified the ring current of **29**. The net current strength of –10.9 nA/T reflects the paratropic ring current of the entire molecule, which is highlighted by yellow lines in the streamline visualization in Figure 20. Meanwhile, the local diatropic ring current of ca. 2.0 nA/T arising from the outer pyrrolic β-β bonds supports the negative NICS(0) values at the centers of pyrrole rings.

The UV/vis/NIR absorption spectrum of **29** is diagnostic of its antiaromatic character, exhibiting broad, ill-defined S band ranging from 600 to 900 nm and intense bands at 477 and 434 nm, which mainly comprise P_1 and P_2 bands (Figure 21). Corresponding to these P bands, strongly coupled Faraday *B* terms with a trough and peak at 476 and 434 nm were observed in the MCD spectrum. The overall absorption and MCD spectral features can be illustrated in terms of Michl's [4N]-perimeter model for antiaromatic compounds. The nodal patterns originating from the 20π-electron [16]annulene ($C_{16}H_{16}^{4-}$) can also be seen for the frontier MOs of **29** (Figure 22).

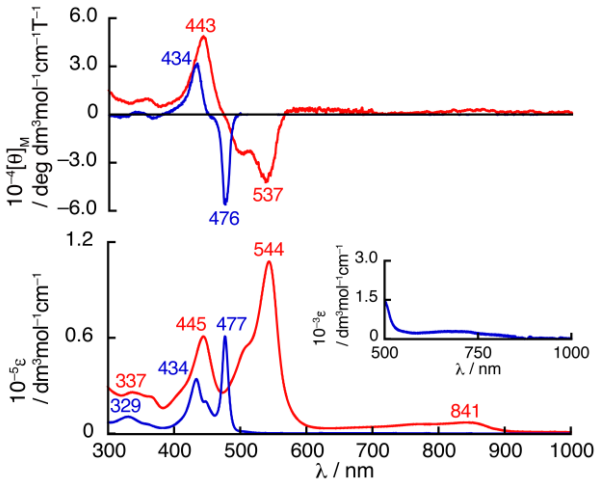

Figure 21. UV/vis/NIR absorption (bottom) and MCD (top) spectra of **29** (blue line) and **30** (red line) in $CHCl_3$. The inset shows the absorption spectrum of **29** in the vis/NIR regions. Redrawn from ref. 67.

In the cyclic voltammetry, **29** exhibited stepwise two one-electron oxidations at 0.05 and 0.68 V (*vs.* Fc^+/Fc), which were ascribed to 20π/19π and 19π/18π redox processes. Despite the attempt to obtain 18π-aromatic dication species as with *N*,*N'*-diaryl-substituted 5,15-diaminoporphyrin, chemical oxidation of **29** with $AgPF_6$ and $NOSbF_6$ provided the corresponding dimer (**30**) and tetrakis-β-nitrated product (**31**), respectively (Scheme 15).[67,68] The structures of these compounds were elucidated by X-ray diffraction analysis (Figure 23). In the structure of **30**, two 5,15-dioxaporphyrin molecules were linked at the β,β-positions, whereas the four β-positions adjacent to the *meso*-oxygen atoms were nitrated in the case of **31**.

The observed reactivities at the β-positions upon oxidation were explained in terms of delocalization of the radical spin densities on the β-positions next to the *meso*-oxygen atoms, which was revealed by electrochemical ESR spectroscopy and DFT calculations. The different reactivities of the 19π-radical cation of **29** from that of *N*,*N'*-diaryl-substituted 5,15-diaminoporphyrin, which simply formed aromatic 18π-dications, despite the similar spin density distribution pattern (Figure 13), can be ascribed to the less

steric hindrance around the β-positions at the *meso*-oxygen side. This can facilitate oxidative coupling reaction to form the dimer and oxidative nitration with nitrosonium ions[69] to form tetrakis-β-nitrated product (Figure 24).

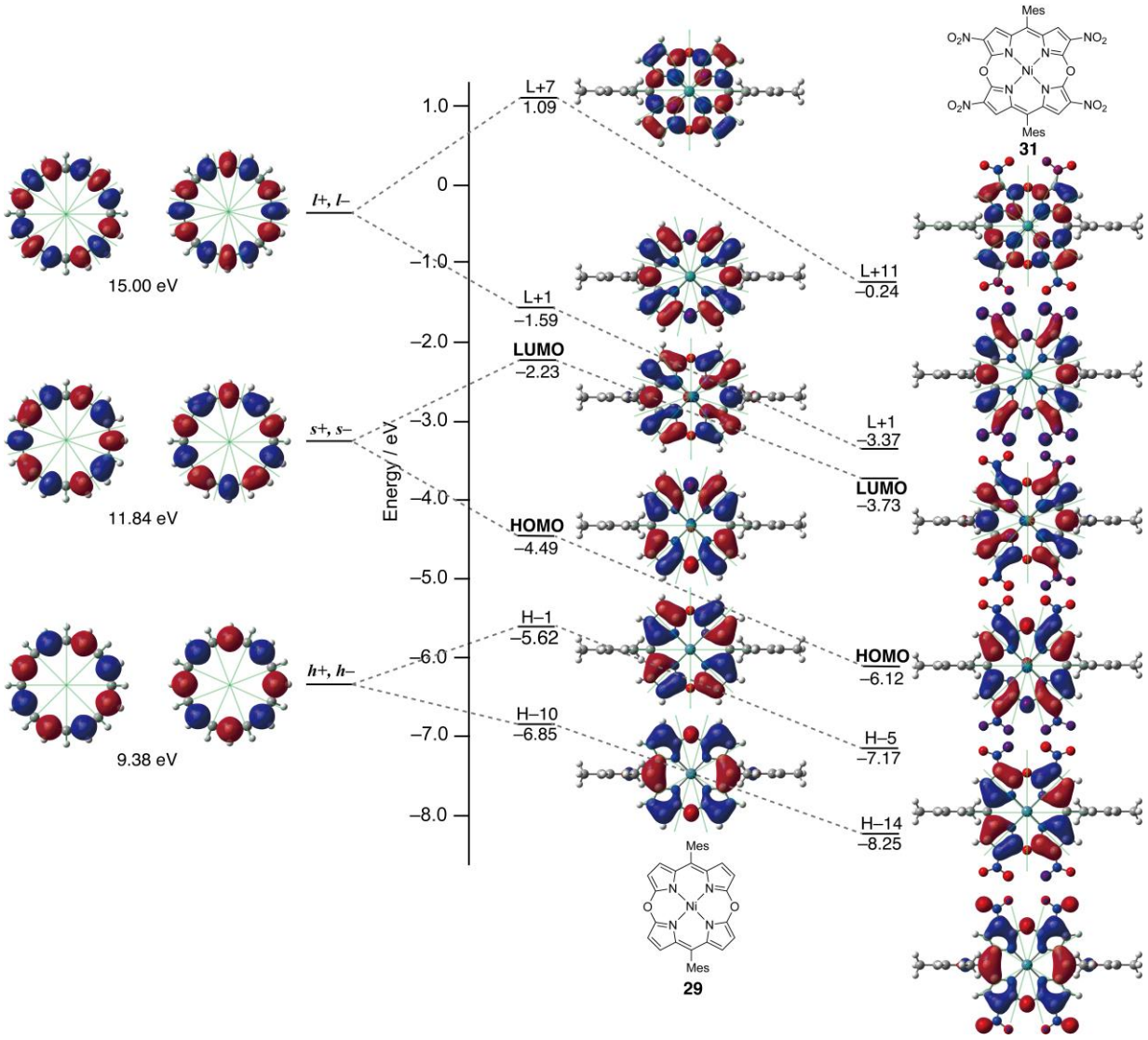

Figure 22. Frontier MO diagrams of **29**, **31**, and 20π-electron [16]annulene ($C_{16}H_{16}^{4-}$) perimeter at the B3LYP/6-31G(d) level. Nodal planes are drawn with pale green lines. Redrawn from ref. 68.

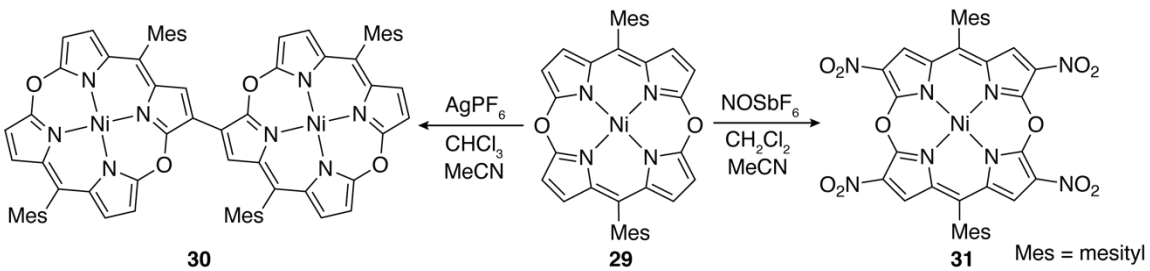

Scheme 15. Synthesis of β,β-linked dimer **30** and tetrakis-β-nitrated 5,15-dioxaporphyrin **31**

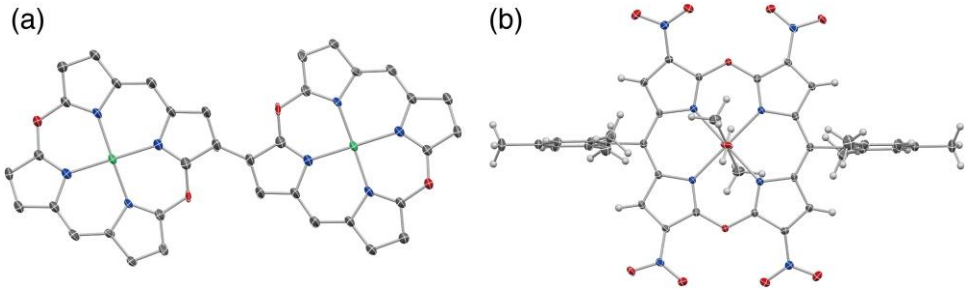

Figure 23. X-Ray single crystal structures of (a) β,β-linked dimer **30** and (b) tetrakis-β-nitrated 5,15-dioxaporphyrin **31**. In the structure of **30**, mesityl substituents and hydrogen atoms are omitted for clarity. The thermal ellipsoids are scaled to the 50% probability level.

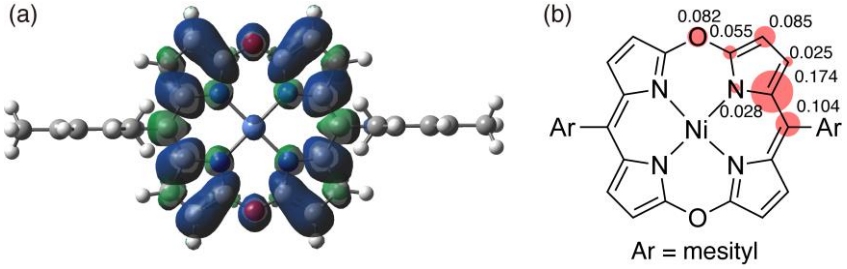

Figure 24. (a) Spin density distribution of the radical cation of **29** and (b) spin densities on its structure calculated by the DFT method at the B3LYP/6-31G(d) level. Redrawn from ref. 67.

The UV/vis/NIR absorption spectrum of the dimer **30** exhibited the red-shift and intensification of the main absorption bands due to the excitonic coupling of the P_1 band, which is supposed to be aligned in a long-molecular axis (Figure 21). Meanwhile, the red-shift was observed for **31** due to stabilization of the frontier MOs by electron-withdrawing nitro groups (Figure 22). Such substituent effect was also observed in the cyclic voltammogram of **31**, exhibiting two pseudoreversible oxidation waves at 1.02 and 1.14 V (*vs*. Fc^+/Fc) and reduction waves at –0.89 and –1.09 V. Despite the significant perturbation by the nitro groups, **31** retains a certain degree of antiaromaticity, which is supported by the ACID plots in addition to the diagnostic ^1H NMR spectrum and UV/vis/NIR absorption spectral profile as an antiaromatic compound (Figure 25).

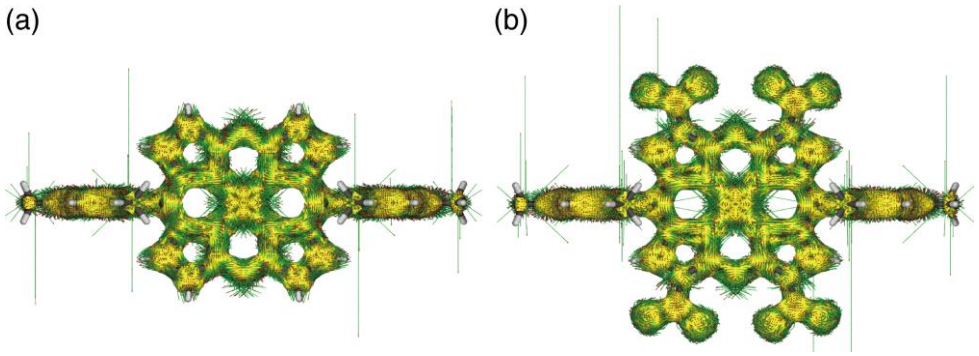

Figure 25. ACID plots of (a) **29** and (b) **31** (isovalue = 0.05). Redrawn from ref. 68.

3-4. 5,15-Dithiaporphyrin

5,15-Dithiaporphyrin was synthesized as a free base form (**32**) in 53% yield by Shinokubo *et al*. from a reaction of a bis(α,α'-dichlorodipyrrin) zinc(II) complex and sodium sulfide hydrate in DMF at 65 ºC (Scheme 16).[70] Along with free base **32**, a small amount of zinc(II) complex **33** was also formed. When a bis(α,α'-dichlorodipyrrin) nickel(II) complex was used instead of the zinc complex, 10-thiacorrole **34** was obtained as a sole product in 41% yield. Later on, Shinokubo *et al*. reported that free base **32** was also synthesized from an α,α'-dibromodipyrrin in the absence of metal templates (Scheme 16).[71]

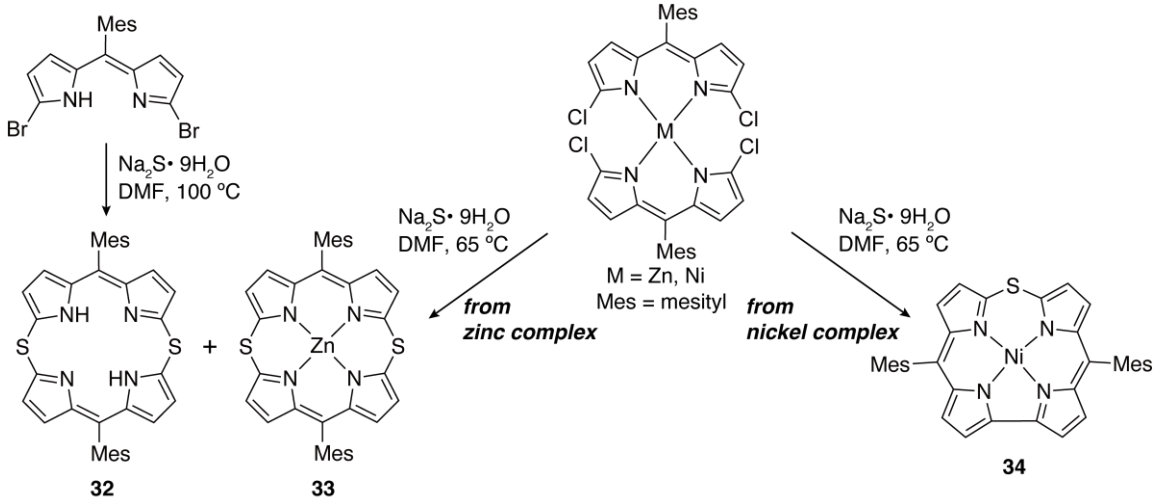

Scheme 16. Synthesis of 5,15-dithiaporphyrin (**32** and **33**) and 10-thiacorrole **34**

Nickel(II) complex of 5,15-dithiaporphyrin **35** was synthesized from metalation of free base **32** with nickel(II) acetylacetonate at room temperature. Other metal ions such as copper(II) (**36**), palladium(II) (**37**), and platinum(II) (**38**) were also inserted in a similar manner (Scheme 17). In contrast to facile metalation at room temperature, nickel insertion at 100 ºC in toluene provided 10-thiacorrole **34** in 43% yield. **34** and its copper(II) analogue (**39**) were also formed by sulfur extraction reaction of **35** and **36** in the presence of triphenylphosphine, whereas no such desulfur reaction was observed for the free base and other metal complexes. Although a similar reaction was reported for a free base and zinc(II) complex of octakis-β-alkyl-substituted 5,15-dithiaporphyrin by Johnson *et al.*, much higher temperature (214 ºC) was required.[72,73] On the basis of the hypothesis that this unique reactivity originates from the smaller size of nickel ion, the thermal reactivity of aluminum(III) complex of 5,15-dithiaporphyrin prepared from **32** and $AlCl_3$ was examined in the presence of triphenylphosphine. As Shinokubo *et al*. expected, a desulfur reaction occurred to provide aluminum(III) complex of 10-thiacorrole **40** (Scheme 17).

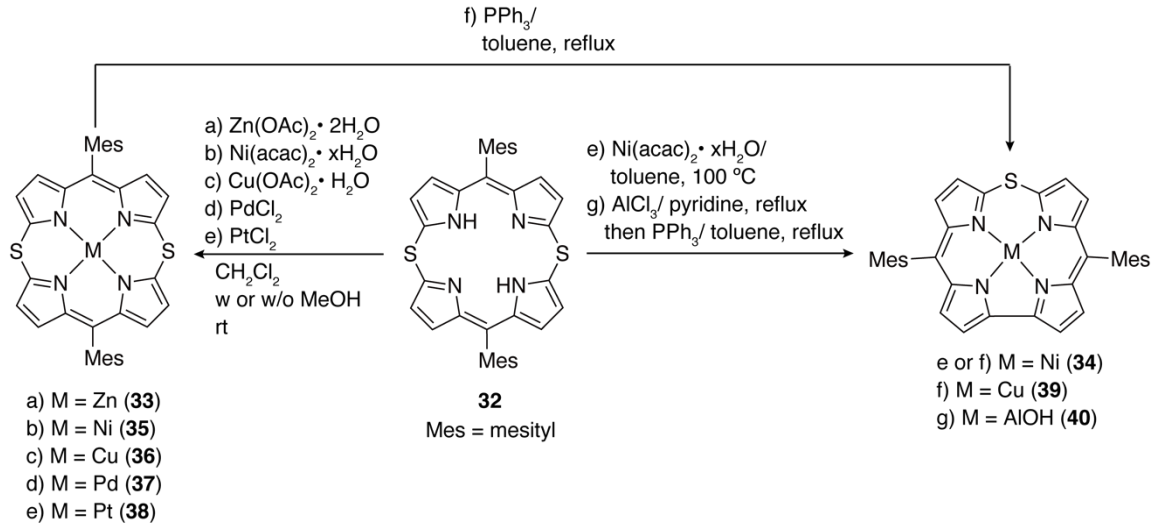

Scheme 17. Metalation and desulfur reaction of 5,15-dithiaporphyrin

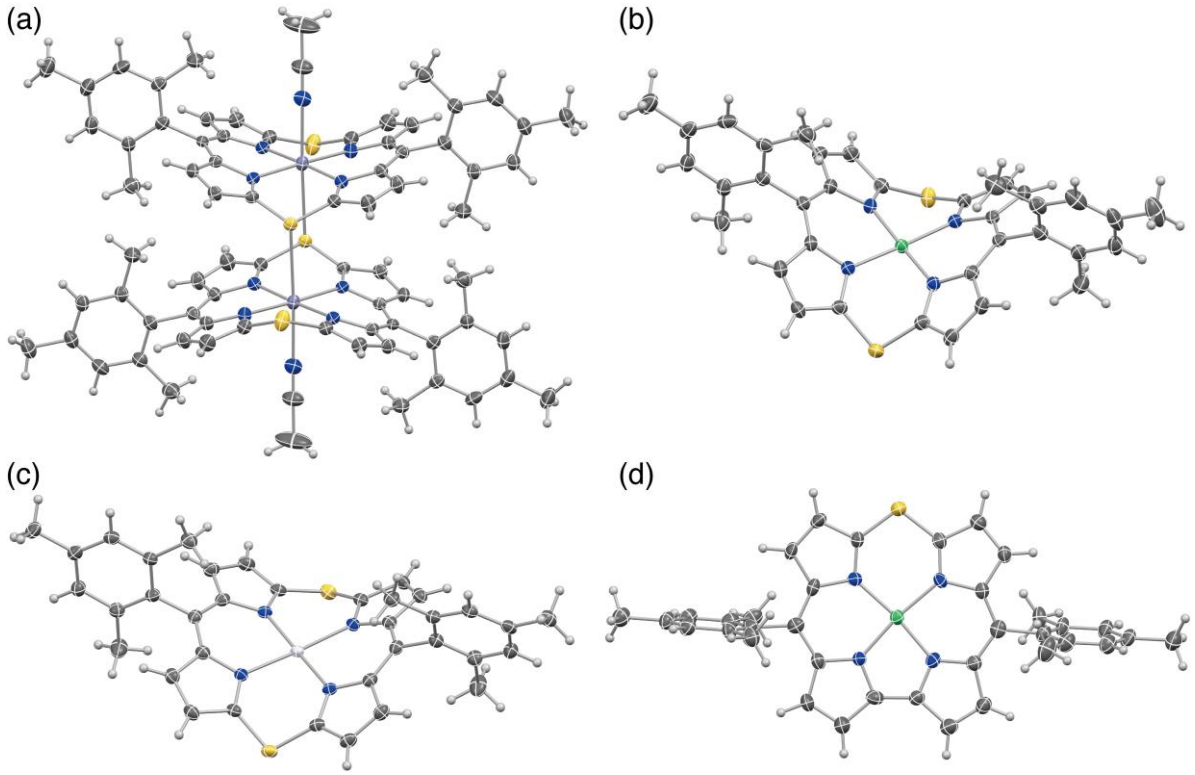

Figure 26. X-Ray single crystal structures of (a) zinc(II) (**33**), (b) nickel(II) (**35**), and (c) platinum(II) (**38**) complexes of 5,15-dithiaporphyrin and (d) nickel(II) complex of 10-thiacorrole **34**. The thermal ellipsoids are scaled to the 50% probability level.

Unlike planar structures of 5,15-diaminoporphyrin and 5,15-dioxaporphyrin, 5,15-dithiaporphyrin exhibited gable structures due to the long C–S bonds (Figure 26). In the cases of the zinc(II) and copper(II) complexes, one of the *meso*-sulfur atoms is bound to the central metal ion of the neighboring molecule to form a stacked dimer (Figure 26a). The bent angle of the two dipyrrin planes is 117.6º for the nickel(II) complex **35**, which is much smaller than those of other metal complexes (**33**: 143.8º, **36**: 135.7º,

and **38**: 134.3º). Because of this significant bending, the distance between sulfur-bridged α-carbon atoms in **35** becomes short, which facilitates carbon–carbon bond formation. The proposed reaction mechanism based on DFT calculations, involving the formation of an episulfide intermediate, sulfur migration, and removal of sulfur by triphenylphosphine, also revealed the critical factor of the bending angle and the α-carbon distance (Scheme 18).

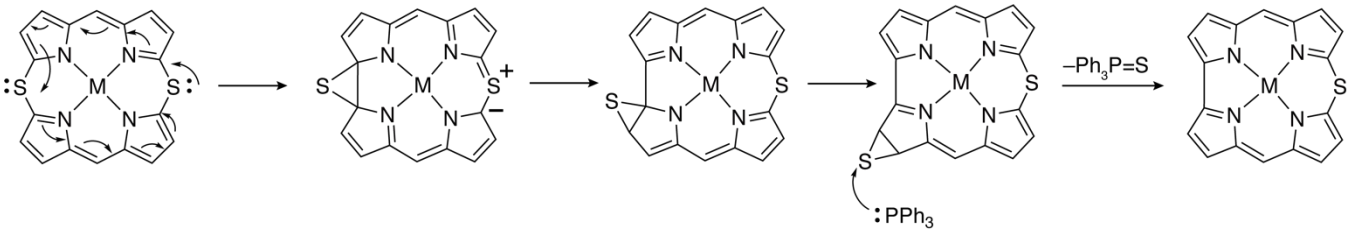

Scheme 18. Proposed desulfur reaction mechanism

Despite the 20π-electron conjugated system, 5,15-dithiaporphyrin is nonaromatic, judging from the chemical shifts of the β-proton at δ = 6.08–6.45 ppm and small positive NICS values. Shinokubo *et al*. ascribed the nonaromaticity of 5,15-dithiaporphyrin to the gable structures due to the long C–S bonds. In contrast, 10-thiacorrole **34** exhibited β-proton signal in the aromatic region at δ = 7.9–8.4 ppm and largely negative NICS values (δ = –15.0 and –11.5 ppm) inside the macrocycle due to the diatropic ring current arising from the 18π-electron aromatic conjugation of a corrole structure. This indicates the effective inclusion of the lone pair in the 3p orbital on the sulfur atom into the macrocyclic conjugation.

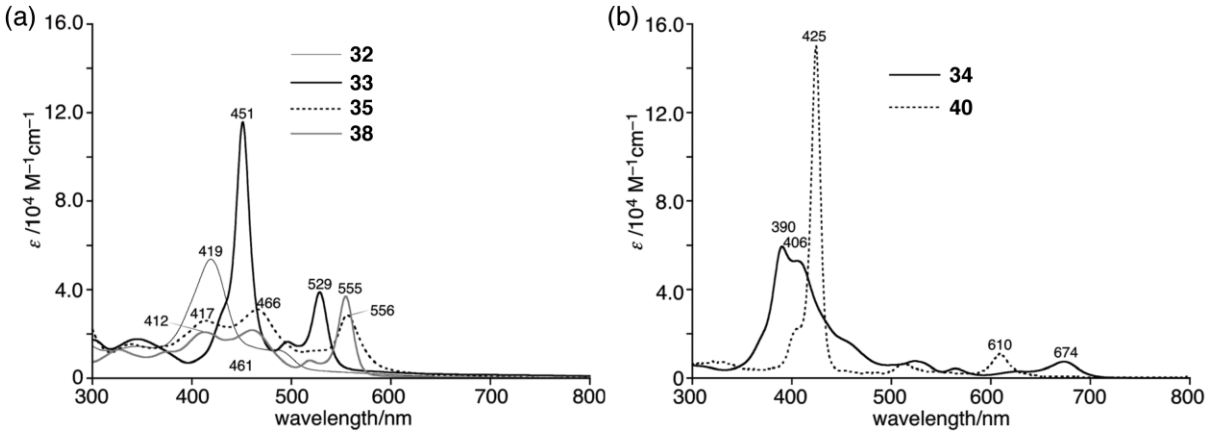

Figure 27. UV/vis absorption spectra of (a) 5,15-dithiaporphyrin (**32**, **33**, **35**, and **38**) and (b) 10-thiacorrole (**34** and **40**) in CH_2Cl_2. Redrawn from ref. 70.

The absorption spectra of 5,15-dithiaporphyrins are similar to those of calix[4]phyrin metal complexes rather than those of antiaromatic porphyrin analogues (Figure 27). The absorption spectral profiles, which vary depending on the central metal ions, can be ascribed to the structural flexibility of the

5,15-dithiaporphyrin ligand, such as a variation of the bending angles observed for the crystal structures. Despite significant broadening, 10-thiacorrole **34** exhibited the porphyrin-like Soret and Q bands. In addition, the narrow electrochemical HOMO–LUMO gap of **34** estimated based on the cyclic voltammograms is also in good agreement with the aromatic nature of 10-thiacorrole.

In analogy with sulfide compounds, 5,15-dithiaporphyrin **32** was oxidized to its sulfone derivative, 5,5,15,15-tetraoxo-5,15-dithiaporphyin **41**, upon treatment with *meta*-chloroperbenzoic acid (*m*CPBA) in dichloromethane (Scheme 19).[74] Metalation of **41** was also examined to provide zinc(II) and nickel(II) complexes (**42** and **43**). Due to the nonaromatic nature, sharp β-proton signals appeared at δ = 6.74 and 6.28 ppm for **41** and at δ = 6.70 and 6.24 ppm for **42**. In contrast, the nickel(II) complex exhibited paramagnetic shifts of pyrrolic proton signals due to the high-spin state of the central hexacoordinate nickel(II) ion with methanol axial ligands. After replacement of the axial methanol with pyridine, the β-proton of **44** resonated as two broad signals in δ = 45–55 ppm. The high-spin ground states of **43** and **44** were also confirmed by the temperature dependent magnetic susceptibility measurement (SQUID), which revealed their spin multiplicity of S = 1 with the χT values of 1.1 emu K mol^{-1} at 300 K. The axial ligands were removed at 35 ºC under high vacuum for 1 h to provide the tetracoordinate nickel(II) complex **45**, which exhibited two sharp β-proton at δ = 7.0 ppm due to the low-spin state of the central nickel(II) ion.

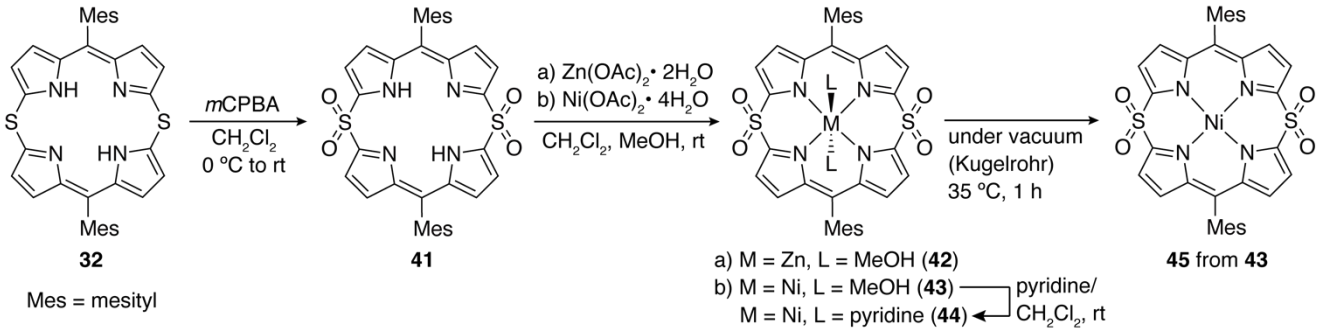

Scheme 19. Synthesis of 5,5,15,15-tetraoxo-5,15-dithiaporphyin

As with the crystal structures of 5,15-dithiaporphyrin, the gable structures with dihedral angles of 117º–129º between two dipyrrin planes were elucidated for the sulfone derivatives (Figure 28). The shorter averaged Ni–N bond lengths of 1.91 Å in **45** than those of the equatorial Ni–N bonds of 2.08 Å for **43** and a derivative of **44** with 4-methylpyridine ligands (**44'**) were ascribed to the smaller ionic radius of the tetracoordinate nickel(II) ion than that of the hexacoordinate one.

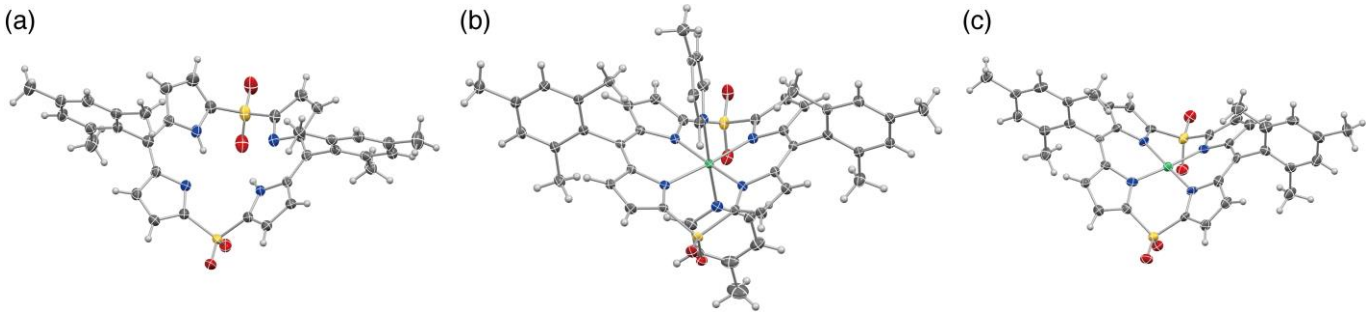

Figure 28. X-Ray single crystal structures of (a) 5,5,15,15-tetraoxo-5,15-dithiaporphyin **41** and its nickel(II) complexes (b) **44'** and (c) **45**. The thermal ellipsoids are scaled to the 50% probability level.

The UV/vis absorption spectrum of free base **41** was broadly similar to that of the corresponding 5,15-dithiaporphyrin **32** (Figure 27), whereas the absorption spectra of the nickel(II) complexes varied depending on the absence or presence of the axial ligands (Figure 29a). On the basis of the Job's plot for titration of pyridine into a dichloromethane solution of **45** (Figure 29b,c), Shinokubo *et al*. revealed 1:1 binding with the binding constant of $2.5(1) \times 10^5$ M^{-1}, which is much higher than that of the electron-deficient porphyrin nickel(II) complexes (10–100 M^{-1}). Moreover, the initial coordination of **44** is strong, whereas the second one is so weak to be unlikely in dilute solution. The identical absorption spectrum of **43** to that of **45** also supported facile liberation of methanol axial ligands in a dilute solution due to weaker coordination of methanol than pyridine.

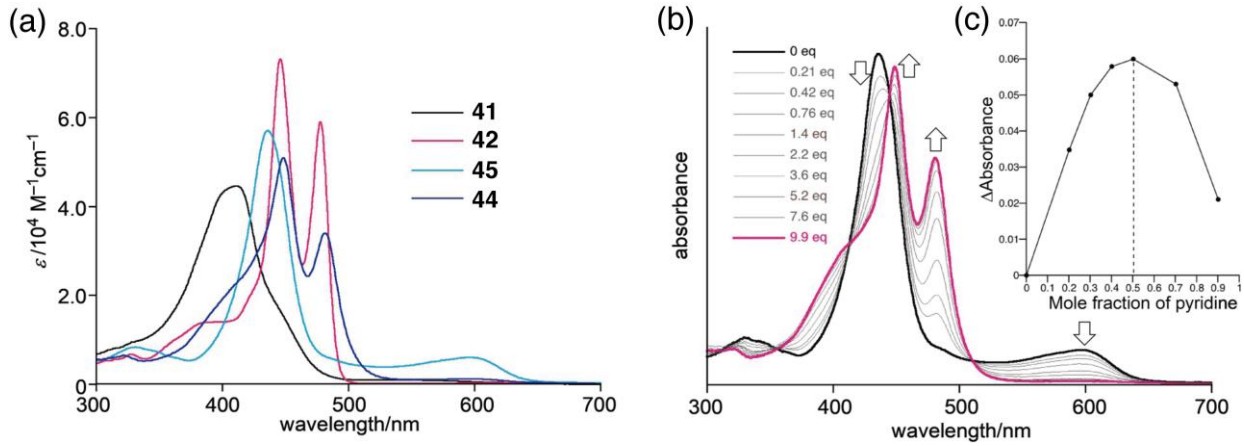

Figure 29. (a) UV/vis absorption spectra of 5,5,15,15-tetraoxo-5,15-dithiaporphyin **41** and its metal complexes (**42**, **44**, and **45**) in CH_2Cl_2. (b) Absorption spectral changes of **45** upon addition of pyridine in a CH_2Cl_2 solution. (c) Job's plot for the complexation of **45** with pyridine. Redrawn from ref. 74.

3-5. 5-Amino-15-chalcogenoporphyrins

5,15-Diheteroporphyrins bearing two types of heteroatoms were synthesized using nitrogen-linked monohalodipyrrin precursors. Matano *et al*. reported the synthesis of 5-amino-15-oxaporphyrin **46** as shown in Scheme 20.[75] Zinc(II) metalation of equimolar amounts of 1,9-dichloro-5-mesityldipyrrin and

1-chloro-9-(4-methoxyphenylamino)-5-mesityldipyrrin afforded three kinds of bisdipyrrin zinc(II) complexes. Among them, the asymmetric complex was isolated and heated in the presence of potassium carbonate to form 1,19-dichloro-5,15-dimesityl-10-(4-methoxyphenyl)-10-azatetrapyrrin. This tetrapyrrin was further reacted with excess 4-methoxybenzaldoxime and NaH to provide 5-amino-15-oxaporphyrin **46**. Although **46** was also oxidized in a stepwise manner to its radical cation **47** and dication **48** (Scheme 20), isolation as solid samples was difficult due to gradual decomposition in concentrated solutions under ambient conditions. This gives contrast to the air stability of the radical cation and dication of 5,15-diaminoporphyrin.

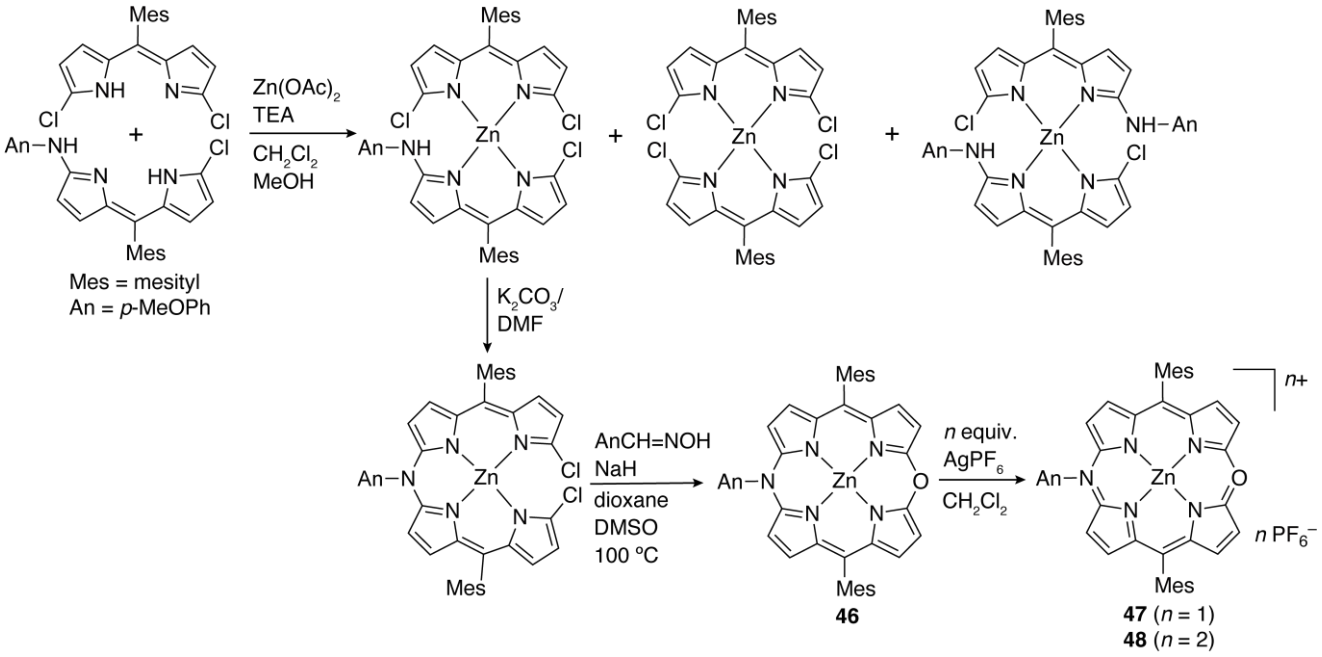

Scheme 20. Synthesis of 5-amino-15-oxaporphyrin **46** and oxidation to 19π-radical cation **47** and 18π-aromatic dication **48**

On the basis of the optimized structures, gradual shortening of the bond lengths between *meso*-nitrogen/oxygen and α-carbon from **46** (1.394/1.358 Å) to **47** (1.381/1.347 Å) and **48** (1.366/1.336 Å) indicated the strengthening of the resonance interactions in this order. The antiaromaticity/aromaticity y of **46** and **48** was estimated by ^{1}H NMR spectroscopy. The β-protons of **46** resonated at δ = 3.8–4.9 ppm due to the paratropic ring current effect, whereas **48** exhibited the β-proton signals at δ = 7.98–8.66 ppm due to the diatropic ring current effect (Figure 30). Although the inductive effect of the heteroatoms should be considered, the slightly smaller paratropic ring current effect of **46** and diatropic ring current effect of **48** than those of the corresponding 5,15-diaminoporphyrin and its dication can be ascribed to the greater electronegativity of oxygen than that of nitrogen, which hampers global delocalization of the lone pair electrons. The less positive and negative NICS(0) values of the model structures of **46** (δ = +5.79

ppm, +7.11, and +6.11 ppm at a, b, and c positions) and **48** (δ = –12.30, –12.31, and –13.42 ppm at a, b, and c positions) than those of 5,15-diaminoporphyrin and its dication, respectively, also supported their weaker antiaromaticity/aromaticity (Figure 31).

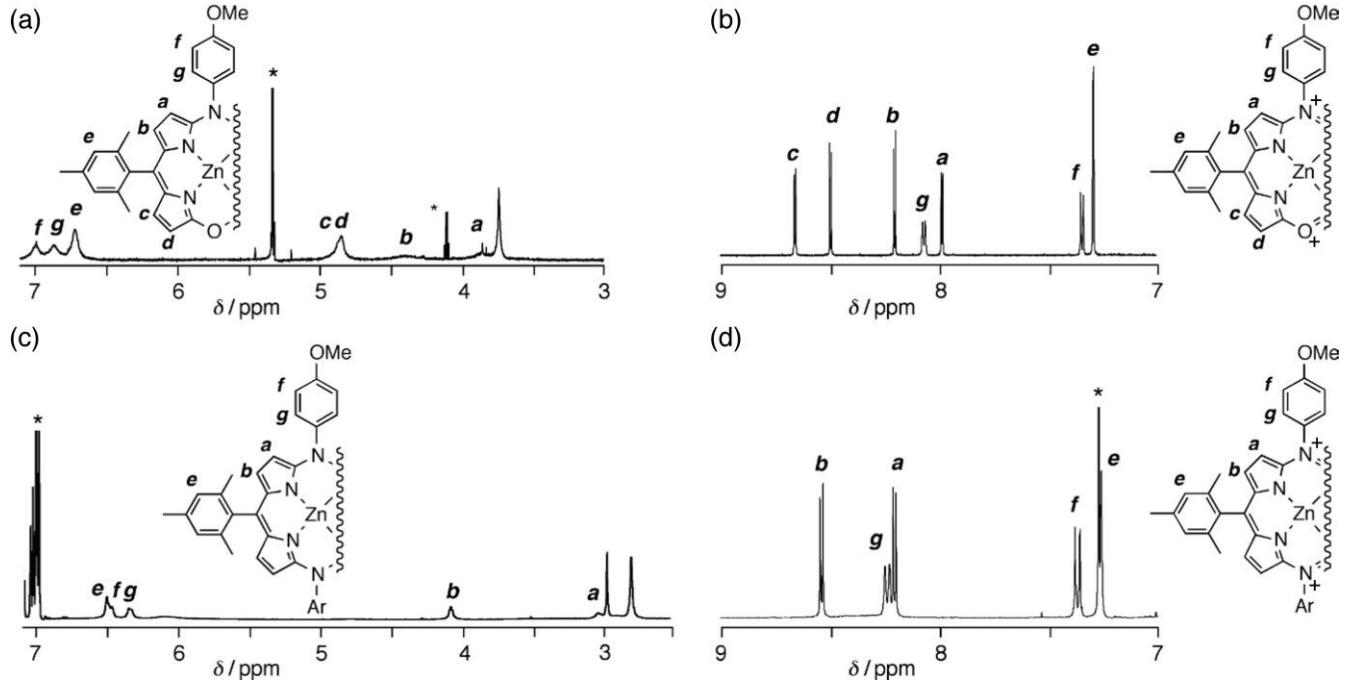

Figure 30. ^{1}H NMR spectra of (a) **46** in CD_2Cl_2, (b) **48** in CD_2Cl_2, (c) 5,15-diaminoporphyrin **14c** in C_6D_6, and (d) dication **15c** in $CDCl_3$. Asterisks indicate residual solvent signals. The spectra were measured with 700 MHz for **46** and **48** and 400 MHz for the 5,15-diaminoporphyrin. Reprinted with permission from ref. 75 Copyright 2018 Wiley.

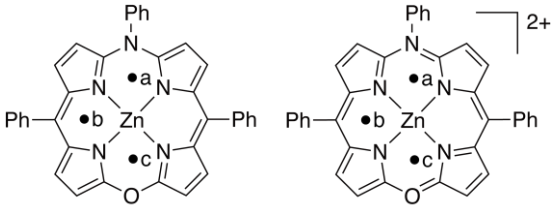

Figure 31. Model structures of **46** and **48**

The cyclic voltammetry measurement on **46** revealed two reversible waves at –0.35 and +0.28 V (*vs.* Fc^+/Fc), which were assigned as the 20π/19π and 19π/18π redox processes (Figure 32). These redox potentials were positively shifted by 0.34–0.36 V from those of the corresponding 5,15-diaminoporphyrin, reflecting the greater electronegativity of oxygen than nitrogen.

The UV/vis/NIR absorption spectrum of 5-amino-15-oxaporphyrin at each oxidation state is diagnostic of their 20π-electron antiaromatic, 19π-electron radical cation, and 18π-electron aromatic states, respectively. Compared with the corresponding 5,15-diaminoporphyrin, the main absorption of **46** at 437

and 488 nm, which can presumably be assigned as P bands, was blue-shifted, whereas the NIR band of **47** at 1034 nm and the Q band of **48** at 671 nm were red-shifted (Figure 33). Upon addition of magic blue to a dichloromethane solution of **46**, the absorption spectrum progressively changed to those of **47** and **48** with several isosbestic points, giving contrast to the oxidation behavior of 5,15-dioxaporphyrin **29**, which formed a dimer by oxidation.[67]

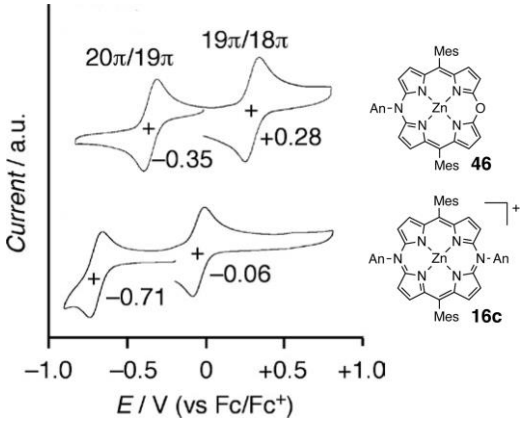

Figure 32. Cyclic voltammograms of 5-amino-15-oxaporphyrin **46** (upper) and 5,15-diaminoporphyrin radical cation **16c** (lower) in CH_2Cl_2 containing 0.1 M Bu_4NPF_6 as a supporting electrolyte at a scan rate of 60 mV s^{-1}. Redrawn from ref. 75.

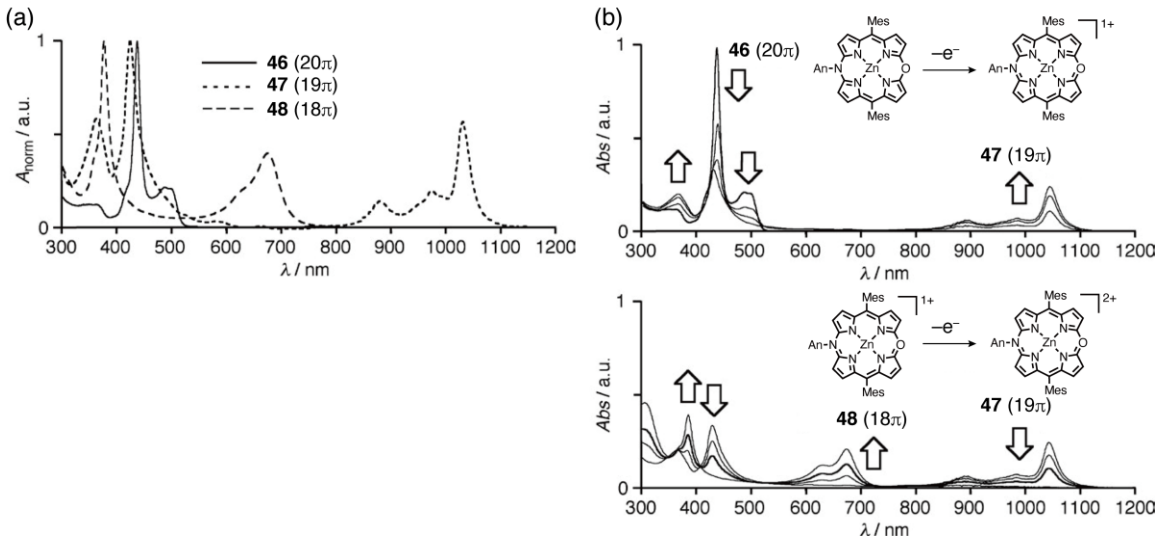

Figure 33. (a) UV/vis/NIR absorption spectra of 5-amino-15-oxaporphyrin **46** and its oxidized species (**47** and **48**) in CH_2Cl_2 and (b) spectral changes upon stepwise oxidation from **46** to **47** (upper) and from **47** to **48** (lower). The counter anion of **47** and **48** was hexachloroantimonate. Redrawn from ref. 75.

5-Amino-15-thiaporphyrin **49** was synthesized by Shinokubo *et al.* from nitrogen-linked monobromodipyrrin [76] in the presence of sodium sulfide in DMF at 65 ºC for 10 h (Scheme 21).[77] In analogy with 5,15-dithiaporphyrin **32**, oxidation of **49** with *m*CPBA provided its sulfone form **50**. Despite the gable structure revealed by X-ray diffraction analysis, upfield shifts of the β-proton signals at δ = 5.97,

5.92, 5.77, and 5.55 ppm from those of 5,15-dithiaporphyrin around δ = 6.3 ppm indicated the presence of the paratropic ring current effect (Figure 34). However, the upfield shifts were substantially smaller than those observed for 5,15-diaminoporphyrin (δ = 3.5–4.6 ppm), indicating weaker antiaromaticity of **49**. The positive NICS values of δ = +10–15 ppm inside the macrocycle and the counterclockwise ring current estimated by the ACID calculations also supported the antiaromaticity of **49**. In contrast, the sulfone derivative **50** was nonaromatic, and the β-proton signals of **50** appeared at δ = 7.42, 7.18, 6.92, and 6.87 ppm. The loss of the lone pair on the sulfur atoms due to the formation of S=O bonds can be attributed to the disappearance of antiaromaticity of **49** upon oxidation.

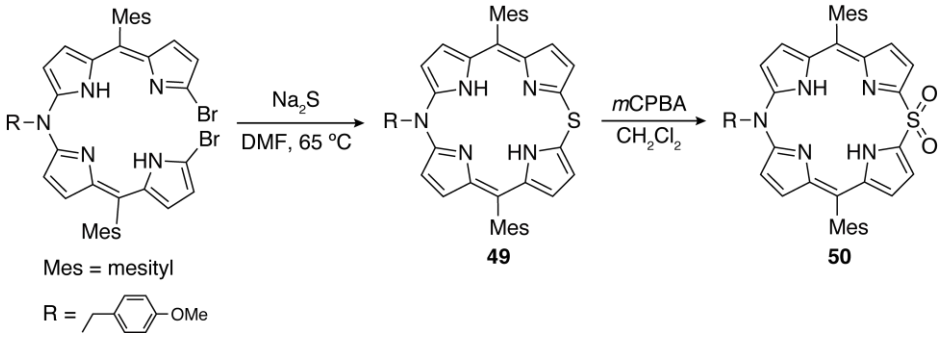

Scheme 21. Synthesis of 5-amino-15-thiaporphyrin **49** and its sulfone derivative (**50**)

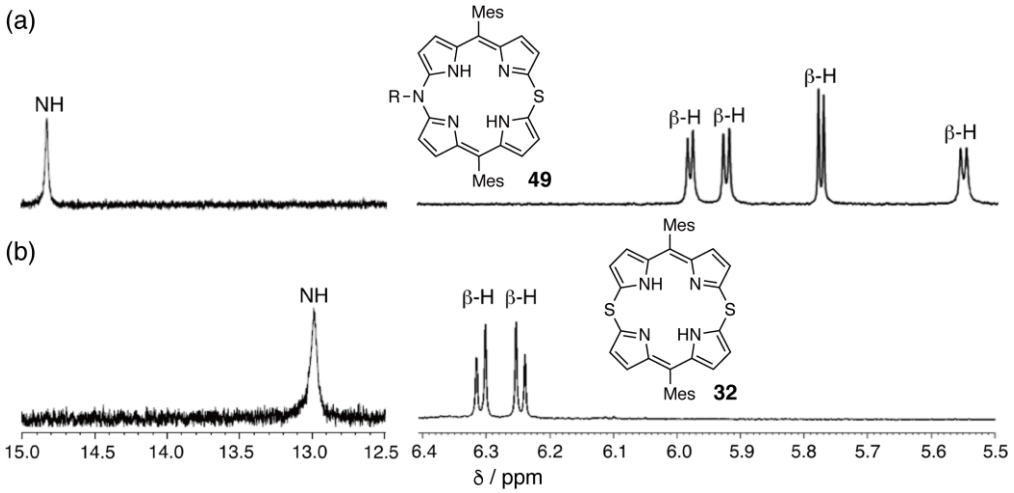

Figure 34. ^{1}H NMR spectra of (a) 5-amino-15-thiaporphyrin **49** and (b) 5,15-dithiaporphyrin **32** in $CDCl_3$. Redrawn from ref. 77.

The UV/vis/NIR absorption spectra of **49** and **50** were characteristic for their antiaromatic and nonaromatic conjugation, respectively (Figure 35). In addition to the intense bands in the visible region, **49** also exhibited the broad, ill-defined S band ranging from 500 to 800 nm, whereas the absorption spectrum of **50** was similar to those of dipyrrin dimers. In contrast to the non-fluorescence of **49**, fluorescence emission was observed for **50**, and the fluorescence quantum yield decreased as the solvent polarity increased.

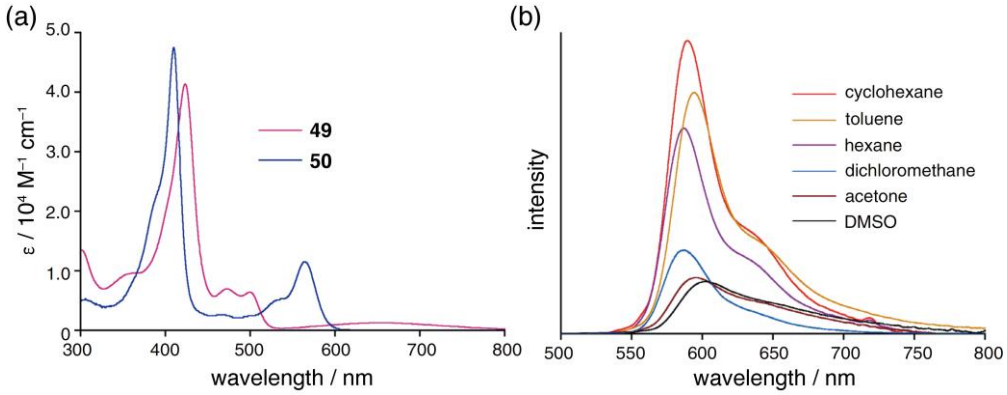

Figure 35. (a) UV/vis/NIR absorption spectra of **49** and **50** and (b) fluorescence spectra of **50** in various solvents. Redrawn from ref. 77.

4. CONCLUSION

In this review, the recent progress in the chemistry of 5,15-diheteroporphyrins synthesized from α,α'-dihalodipyrrins is summarized. The facile synthesis of α,α'-dihalodipyrrins and their reactivity toward nucleophilic substitution reaction has enabled easy access to this type of heteroporphyrins. Except for nonaromatic 5,15-dithiaporphyrin, 5,15-diheteroporphyrins bearing amino-nitrogen or chalcogen atoms or both are 20π-electron antiaromatic due to successful incorporation of lone pair into the conjugated system of the porphyrin skeleton. The degree of antiaromaticity estimated based on the chemical shifts of the β-protons in the ^{1}H NMR spectra and the NICS values inside the macrocycle decreases in the order of 5,15-diaminoporphyrin > 5-amino-15-oxaporphyrin > 5,15-dioxaporphyrin ≈ 5-amino-15-thiaporphyrin. The weaker antiaromaticity of oxygen-containing 5,15-diheteroporphyrins than 5,15-diaminoporphyrin can be ascribed to the greater electronegativity of oxygen than nitrogen, which hampers incorporation of the lone pair to the global conjugation, whereas the gable structures caused by the long C–S bonds for sulfur-containing ones interrupts the macrocyclic conjugation. Despite the relatively weak antiaromaticity compared with other antiaromatic porphyrin analogues such as norcorrole,[78] the high stability of these series of 5,15-diheteroporphyrins is a potential property for further studies toward molecular electronics application, where high molecular conductivity can be expected because of the inherently small HOMO–LUMO gaps of antiaromatic compounds. Further synthetic study will enrich the variety of heteroporphyrin analogues. In addition, post-functionalization of 5,15-diheteroporphyrins is also indispensable for fine-tuning of their optical and electronic properties. Research along these directions will be accomplished in the near future.

ACKNOWLEDGEMENTS

This work was supported by Grants-in-Aid for Scientific Research (B) (JSPS KAKENHI Grant no. JP19H02703), Challenging Exploratory Research (JSPS KAKENHI Grant no. JP18K19081) and Scientific Research on Innovative Area, ‘‘π-System Figuration: Control of Electron and Structural

Dynamism for Innovative Functions (no. 2601)'' (JSPS KAKENHI Grant no. JP15H01001 and JP17H05160).

REFERENCES

1. Heme Biochemistry in 'Handbook of Porphyrin Science', Vol. 26, ed. by K. M. Kadish, K. M. Smith, and R. Guilard, World Scientific, Singapore, 2013.
2. Chlorophyll, Photosynthesis and Bio-inspired Energy in 'Handbook of Porphyrin Science', Vol. 28, ed. by K. M. Kadish, K. M. Smith, and R. Guilard, World Scientific, Singapore, 2013.
3. Heme Proteins — Part II in 'Handbook of Porphyrin Science', Vol. 30, ed. by K. M. Kadish, K. M. Smith, and R. Guilard, World Scientific, Singapore, 2013.
4. P. R. O. de. Montellano and K. Auclair, 'The Porphyrin Handbook', Vol. 12, ed. by K. M. Kadish, K. M. Smith, and R. Guilard, Academic Press, San Diego, 2000, pp. 183–210.
5. A. H. Jackson, G. W. Kenner, and K. M. Smith, *J. Chem. Soc. C*, 1968, 302.
6. J. H. Fuhrhop, S. Besecke, J. Subramanian, C. Mengersen, and D. Riesner, *J. Am. Chem. Soc.*, 1975, **97**, 7141.
7. S. Besecke and J.-H. Fuhrhop, *Angew. Chem., Int. Ed. Engl.*, 1974, **13**, 150.
8. J.-H. Furhop, A. Salek, J. Subramanian, C. Mengersen, and S. Besecke, *Justus Liebigs Ann. Chem.*, 1975, 1131.
9. S. Saito and H. A. Itano, *J. Chem. Soc., Perkin Trans. 1*, 1986, 1.
10. S. Saito and N. Tamura, *Bull. Chem. Soc. Jpn.*, 1987, **60**, 4037.
11. S. Saito, S. Sumita, K. Iwai, and H. Sano, *Bull. Chem. Soc. Jpn.*, 1988, **61**, 3539.
12. J.-H. Fuhrhop, P. Krüger, and W. S. Sheldrick, *Justus Liebigs Ann. Chem.*, 1977, 339.
13. J.-H. Fuhrhop and P. Krüger, *Justus Liebigs Ann. Chem.*, 1977, 360.
14. A. L. Balch, F. L. Bowles, and L. P. Samankumara, 'Handbook of Porphyrin Science', Vol. 8, ed. by K. M. Kadish, K. M. Smith, and R. Guilard, World Scientific, Singapore, 2010, pp. 293–342.
15. A. L. Balch, L. Latos-Grażyński, B. C. Noll, M. M. Olmstead, L. Szterenberg, and N. Safari, *J. Am. Chem. Soc.*, 1993, **115**, 1422.
16. A. L. Balch, M. Mazzanti, and M. M. Olmstead, *J. Chem. Soc., Chem. Commun.*, 1994, 269.
17. R. Koerner, L. Latos-Grażyński, and A. L. Balch, *J. Am. Chem. Soc.*, 1998, **120**, 9246.
18. A. L. Balch, M. Mazzanti, T. N. St. Claire, and M. M. Olmstead, *Inorg. Chem.*, 1995, **34**, 2194.
19. T. Yamauchi, T. Mizutani, K. Wada, S. Horii, H. Furukawa, S. Masaoka, H.-C. Chang, and S. Kitagawa, *Chem. Commun.*, 2005, 1309.
20. R. Nakamura, K. Kakeya, N. Furuta, E. Muta, H. Nishisaka, and T. Mizutani, *J. Org. Chem.*, 2011, **76**, 6108.

21. K. Kakeya, A. Nakagawa, T. Mizutani, Y. Hitomi, and M. Kodera, *J. Org. Chem.*, 2012, **77**, 6510.
22. A. W. Johnson, I. T. Kay, and R. Rodrigo, *J. Chem. Soc.*, 1963, 2336.
23. Y. Matano, T. Shibano, H. Nakano, and H. Imahori, *Chem. Eur. J.*, 2012, **18**, 6208.
24. M. Horie, Y. Hayashi, S. Yamaguchi, and H. Shinokubo, *Chem. Eur. J.*, 2012, **18**, 5919.
25. Y. Matano, *Chem. Rev.*, 2017, **117**, 3138.
26. B. K. Reddy, A. Basavarajappa, M. D. Ambhore, and V. G. Anand, *Chem. Rev.*, 2017, **117**, 3420.
27. J. L. Sessler, R. S. Zimmerman, C. Bucher, V. Kral, and B. Andrioletti, *Pure Appl. Chem.*, 2001, **73**, 1041.
28. A. N. Cammidge, M. J. Cook, D. L. Hughes, F. Nekelson, and M. Rahman, *Chem. Commun.*, 2005, 930.
29. A. N. Cammidge, I. Chambrier, M. J. Cook, D. L. Hughes, M. Rahman, and L. Sosa-Vargas, *Chem. Eur. J.*, 2011, **17**, 3136.
30. J. Mack, L. Sosa-Vargas, S. J. Coles, G. J. Tizzard, I. Chambrier, A. N. Cammidge, M. J. Cook, and N. Kobayashi, *Inorg. Chem.*, 2012, **51**, 12820.
31. A. Díaz-Moscoso, G. J. Tizzard, S. J. Coles, and A. N. Cammidge, *Angew. Chem. Int. Ed.*, 2013, **52**, 10784.
32. A. van As, C. C. Joubert, B. E. Buitendach, E. Erasmus, J. Conradie, A. N. Cammidge, I. Chambrier, M. J. Cook, and J. C. Swarts, *Inorg. Chem.*, 2015, **54**, 5329.
33. M. Umetani, G. Kim, T. Tanaka, D. Kim, and A. Osuka, *J. Org. Chem.*, 2020, **85**, 3849.
34. M. Umetani, T. Tanaka, and A. Osuka, *J. Porphyrins Phthalocyanines*, 2020, DOI: 10.1142/S1088424619501827
35. Y. Matano, T. Shibano, H. Nakano, Y. Kimura, and H. Imahori, *Inorg. Chem.*, 2012, **51**, 12879.
36. Y. Matano, D. Fujii, T. Shibano, K. Furukawa, T. Higashino, H. Nakano, and H. Imahori, *Chem. Eur. J.*, 2014, **20**, 3342.
37. S. Omomo, Y. Maruyama, K. Furukawa, T. Furuyama, H. Nakano, N. Kobayashi, and Y. Matano, *Chem. Eur. J.*, 2014, **21**, 2003.
38. S. Shimizu, Y. Ito, K. Oniwa, S. Hirokawa, Y. Miura, O. Matsushita, and N. Kobayashi, *Chem. Commun.*, 2012, **48**, 3851.
39. Z. Chen, C. S. Wannere, C. Corminboeuf, R. Puchta, and P. von. R. Schleyer, *Chem. Rev.*, 2005, **105**, 3842.
40. D. Geuenich, K. Hess, F. Köhler, and R. Herges, *Chem. Rev.*, 2005, **105**, 3758.
41. D. Sundholm, H. Fliegl, and R. J. F. Berger, *WIREs Comput. Mol. Sci.*, 2016, 1.
42. R. R. Valiev, I. Benkyi, Y. V. Konyshev, H. Fliegl, and D. Sundholm, *J. Phys. Chem. A*, 2018, **122**, 4756.

43. M. Gouterman, *J. Chem. Phys.*, 1959, **30**, 1139.
44. M. Gouterman, *J. Mol. Spectrosc.*, 1961, **6**, 138.
45. N. Kobayashi, A. Muranaka, and J. Mack, Circular Dichroism and Magnetic Circular Dichroism Spectroscopy for Organic Chemists, Royal Society of Chemistry, UK, 2012.
46. J. Mack, M. J. Stillman, and N. Kobayashi, *Coord. Chem. Rev.*, 2007, **251**, 429.
47. N. Kobayashi and K. Nakai, *Chem. Commun.*, 2007, 4077.
48. J. Mack and N. Kobayashi, *Chem. Rev.*, 2011, **111**, 281.
49. J. Michl, *J. Am. Chem. Soc.*, 1978, **100**, 6801.
50. J. Michl, *Tetrahedron*, 1984, **40**, 3845.
51. J. Michl, *Pure Appl. Chem.*, 1980, **52**, 1549.
52. J. D. Keegan, A. M. Stolzenberg, Y. C. Lu, R. E. Linder, G. Barth, A. Moscowitz, E. Bunnenberg, and C. Djerassi, *J. Am. Chem. Soc.*, 1982, **104**, 4305.
53. A. Kaito, T. Nozawa, T. Yamamoto, M. Hatano, and Y. Orii, *Chem. Phys. Lett.*, 1977, **52**, 154.
54. A. Muranaka, O. Matsushita, K. Yoshida, S. Mori, M. Suzuki, T. Furuyama, M. Uchiyama, A. Osuka, and N. Kobayashi, *Chem. Eur. J.*, 2009, **15**, 3744.
55. M. G. P. M. S. Neves, R. M. Martins, A. C. Tomé, A. J. D. Silvestre, A. M. S. Silva, V. Félix, J. A. S. Cavaleiro, and M. G. B. Drew, *Chem. Commun.*, 1999, 385.
56. T. Tanaka and A. Osuka, *Chem. Rev.*, 2017, **117**, 2584.
57. U. Höweler, J. W. Downing, J. Fleischhauer, and J. Michl, *J. Chem. Soc., Perkin Trans. 2*, 1998, 1101.
58. J. Fleischhauer, U. Höweler, and J. Michl, *J. Phys. Chem. A*, 2000, **104**, 7762.
59. J. Fleischhauer, U. Höweler, J. Spanget-Larsen, G. Raabe, and J. Michl, *J. Phys. Chem. A*, 2004, **108**, 3225.
60. A. Yamaji, H. Tsurugi, Y. Miyake, K. Mashima, and H. Shinokubo, *Chem. Eur. J.*, 2016, **22**, 3956.
61. T. Sugai, M. Minoura, H. Nakano, and Y. Matano, *Bull. Chem. Soc. Jpn.*, 2018, **91**, 1264.
62. T. Satoh, M. Minoura, H. Nakano, K. Furukawa, and Y. Matano, *Angew. Chem. Int. Ed.*, 2016, **55**, 2235.
63. K. Sudoh, T. Satoh, T. Amaya, K. Furukawa, M. Minoura, H. Nakano, and Y. Matano, *Chem. Eur. J.*, 2017, **23**, 16364.
64. K. Murakami, Y. Yamamoto, H. Yorimitsu, and A. Osuka, *Chem. Eur. J.*, 2013, **19**, 9123.
65. K. Sudoh, Y. Satoh, K. Furukawa, H. Nakano, and Y. Matano, *J. Porphyrins Phthalocyanines*, 2020, **24**, 286.
66. K. Sudoh, T. Hatakeyama, K. Furukawa, H. Nakano, and Y. Matano, *J. Porphyrins Phthalocyanines*, 2018, **22**, 542.

67. A. Nishiyama, M. Fukuda, S. Mori, K. Furukawa, H. Fliegl, H. Furuta, and S. Shimizu, *Angew. Chem. Int. Ed.*, 2018, **57**, 9728.
68. A. Nishiyama, Y. Tanaka, S. Mori, H. Furuta, and S. Shimizu, *J. Porphyrins Phthalocyanines*, 2020, **24**, 355.
69. E. K. Kim and J. K. Kochi, *J. Org. Chem.*, 1989, **54**, 1692.
70. H. Kamiya, T. Kondo, T. Sakida, S. Yamaguchi, and H. Shinokubo, *Chem. Eur. J.*, 2012, **18**, 16129.
71. N. Wachi, T. Kondo, S. Ito, S. Hiroto, J.-Y. Shin, and H. Shinokubo, *J. Porphyrins Phthalocyanines*, 2014, **18**, 675.
72. M. J. Broadhurst, R. Grigg, and A. W. Johnson, *J. Chem. Soc., Chem. Commun.*, 1969, 23.
73. M. J. Broadhurst, R. Grigg, and A. W. Johnson, *J. Chem. Soc., Perkin Trans. 1*, 1972, 1124.
74. A. Yagi, T. Kondo, D. Yamashita, N. Wachi, H. Omori, N. Fukui, T. Ikeue, and H. Shinokubo, *Chem. Eur. J.*, 2019, **25**, 15580.
75. K. Sudoh, K. Furukawa, H. Nakano, S. Shimizu, and Y. Matano, *Heteroat. Chem.*, 2018, **8**, e21456.
76. H. Omori, S. Hiroto, and H. Shinokubo, *Chem. Commun.*, 2016, **52**, 3540.
77. D. Yamashita, H. Omori, N. Fukui, and H. Shinokubo, *J. Porphyrins Phthalocyanines*, 2020, **24**, 84.
78. T. Ito, Y. Hayashi, S. Shimizu, J.-Y. Shin, N. Kobayashi, and H. Shinokubo, *Angew. Chem. Int. Ed.*, 2012, **51**, 8542.

Soji Shimizu was born in Kyoto, Japan, in 1979. He graduated from Kyoto University in 2002 and obtained his PhD there under the supervision of Professor Atsuhiro Osuka in 2007 for his research on the syntheses and properties of expanded porphyrins. During his PhD studies, he made a short stay in the group of Professor Jonathan L. Sessler, the University of Texas at Austin in 2005. He was appointed as an assistant professor in 2006 and a lecturer in 2010 at Department of Chemistry, Graduate School of Science, Tohoku University and started his academic career in the group of Professor Nagao Kobayashi in the field of phthalocyanine chemistry. He was then promoted to an associate professor at Department of Chemistry and Biochemistry, Graduate School of Engineering, Kyushu University in 2014. His research interests cover the synthesis of conjugated molecules with novel structures and their optical and electrochemical properties.